

Article

Scale Factor Determination for the GRACE-Follow On Laser Ranging Interferometer including Thermal Correction

Malte Misfeldt ^{1*} , Vitali Müller ¹ , Laura Müller ¹, Henry Wegener ¹ and Gerhard Heinzel ¹ 

¹ Max-Planck-Institut für Gravitationsphysik (Albert-Einstein-Institut) and Institut für Gravitationsphysik, Leibniz Universität Hannover, Callinstraße 38, D-30167 Hannover, Germany

* Correspondence: malte.misfeldt@aei.mpg.de

Abstract: The GRACE Follow-On satellites carry the very first inter-spacecraft Laser Ranging Interferometer (LRI). After more than four years in orbit, the LRI does well in challenging the conventional Microwave Instrument (MWI). However, in the current data processing scheme, the LRI product still needs the MWI data to co-estimate the unknown absolute laser frequency, representing the “ruler” for converting the raw phase measurements into a physical displacement in meters. In this paper, we derive formulas for precisely converting the phase measurement into a range, giving rise to a varying carrier frequency. Furthermore, the dominant errors due to knowledge uncertainty of the carrier frequency as well as uncorrected time biases are derived. In the second part, we address the dependency of the LRI on the MWI in the currently employed cross-calibration scheme and present three different models for the LRI laser frequency, two of which are largely independent of the MWI. Furthermore, we analyze the contribution of thermal variations on the scale factor estimates and the LRI-MWI residuals. A linear model called Thermal Correction (TC) is derived that significantly reduces the differences between LRI and MWI to a level where the MWI observations limit the comparison.

Keywords: GRACE Follow-On; Laser Ranging Interferometer; Scale Factor; Tone Error; Thermal Correction



Citation: Misfeldt, M.; Müller, V.; Müller, L.; Wegener, H.; Heinzel, G. Scale Factor Determination for the GRACE-Follow On Laser Ranging Interferometer including Thermal Correction. *Preprints* **2022**, *1*, 0. <https://doi.org/>

Publisher's Note: MDPI stays neutral with regard to jurisdictional claims in published maps and institutional affiliations.



Copyright: © 2022 by the authors. Licensee MDPI, Basel, Switzerland. This article is an open access article distributed under the terms and conditions of the Creative Commons Attribution (CC BY) license (<https://creativecommons.org/licenses/by/4.0/>).

1. Introduction

The joint U.S.-German gravity space mission GRACE Follow-On (GRACE-FO) follows its successful predecessor, the Gravity Recovery And Climate Experiment (GRACE). The twin satellites were launched on the 22nd of May 2018, and the Laser Ranging Interferometer (LRI) was successfully commissioned in mid-June 2018 [1]. Following the basic concept and design of the predecessor mission, its main scientific instrument for inter-satellite distance measurements is the K-band Ranging (KBR) (or Microwave Instrument, MWI) alongside the accelerometers to determine and remove non-gravitational accelerations acting on the two spacecraft. Global observations of Earth’s gravitational potential and its variations from space allow valuable insights into the hydrological cycle, including rainfall, droughts, ice-melting, and sea-level rise [2].

New to GRACE-FO is the LRI, a technology demonstrator to prove the feasibility of laser interferometry for distance measurements between two spacecraft flying a few hundred kilometers apart. The LRI shows drastically increased precision compared to the KBR instrument [1,3]. Based on the flawless in-orbit operation for over four years and without any degradation observed so far, the LRI technology is now being adopted to serve as the primary instrument in future missions like Next Generation Gravity Mission (NGGM) and Mass Change Mission (MCM) [4–6]. This includes for example changes with respect to reliability and redundancy. Moreover, the success in demonstrating inter-spacecraft laser interferometry was a milestone for the space-based gravitational wave observatory LISA [7].

The LRI has shown very low noise in the inter-satellite ranging measurement of about $0.3 \text{ nm} / \sqrt{\text{Hz}}$ at Fourier frequencies of 1 Hz [1], which is about three orders of magnitude below

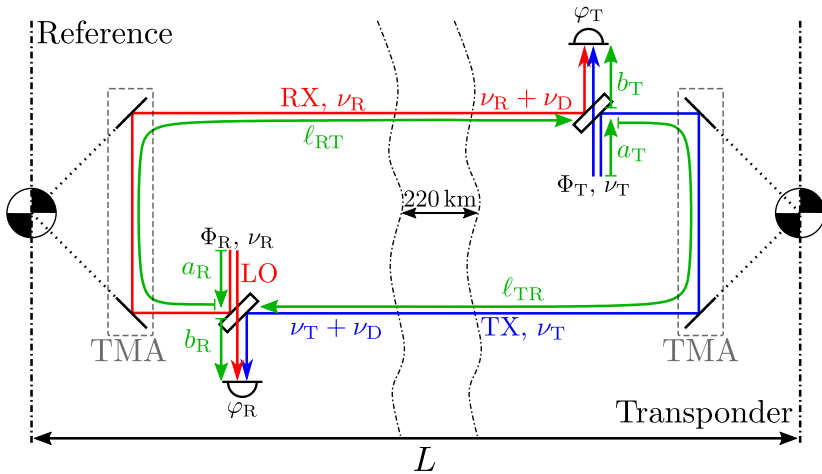


Figure 1. Simplified light paths and frequencies within the LRI.

the noise of the MWI. However, to form the LRI ranging signal, the conversion factor between the raw phase measurement and the desired displacement is needed. This conversion factor is the wavelength $\lambda = c_0 / \nu_R$, with c_0 denoting the speed of light in vacuum and ν_R the optical frequency of the light beam that travels between the spacecraft. The LRI laser frequency on the reference satellite ν_R is actively stabilized to a resonance of an optical reference cavity using the Pound-Drever-Hall (PDH) technique. The jitter of the cavity's resonance frequency mainly depends on the resonator's thermal stability, while the frequency's absolute value can not be measured directly in flight. Therefore, the current data processing scheme foresees a cross-calibration of LRI and KBR to determine the relative scaling between the KBR range and LRI range, using an initial estimate ν_0 for the laser frequency. Through rescaling the initial value ν_0 , the true laser frequency is approximated as $\nu_{\text{estim.}} = \nu_0 / (1 + \varepsilon_{\text{SCF}})$.

This paper aims to investigate approaches to decrease the dependency of the LRI data on KBR data in case the latter breaks and to study the performance of a possible LRI-only NGGM. Therefore, we develop different models for estimating the LRI laser frequency in-flight. Since these models do not minimize the residuals sufficiently, a potential influence of thermal variations into the ranging data is investigated and modelled.

In section 2 we briefly cover the working principle of the LRI and introduce the instrument's most important optical and radiofrequency measures. Section 3 derives the relativistic phase observable, while the phase conversion into range is done in section 4. The dominant error sources of this approach, which apply to actual data processing, are discussed in section 5. Actual flight data is processed in section 6, where we analyze the KBR-LRI cross-calibration method and discuss a frequency change of the cavity resonance onboard GF-1. The derivation and calibration of a telemetry-based absolute laser frequency model is presented in sections 7 and 8 and an empirical correction to this model is derived in section 9. In section 10, the frequency models are used to derive three independent LRI1B-equivalent ranging data sets, which are then compared to each other and to the KBR. In the end, Section 11 focuses on minimizing variations in the relative scale and timeshift of LRI and KBR by reducing thermally-induced measurement errors, also known as tone errors. Coupling factors are derived to model this effect and subtract it from the ranging data. A brief discussion of available technologies to determine the absolute laser frequency for future gravity missions is taken out in section 12 and the findings are concluded in section 13.

2. Working Principle of LRI

The LRI is set up in an active-transponder configuration [8], the principle of which is shown in fig. 1. Both spacecraft receive and emit light. They are equally equipped with photoreceivers to measure the interference between the incoming and local light fields (shown in red and blue in fig. 1). The LRI is a heterodyne Mach-Zehnder type interferometer, meaning that the two interfering light fields have slightly different optical frequencies, which produces an interference beatnote at the difference frequency. This beatnote frequency is roughly 10 MHz for the LRI.

On the reference side, the laser frequency ν_R is stabilized by means of an optical reference cavity using the PDH technique [9]. The residual frequency fluctuations $\delta\nu_R$ were required to be below $30\text{ Hz}/\sqrt{\text{Hz}}$ for Fourier frequencies above 10 mHz, with a relaxation towards lower Fourier frequencies to account for thermal noise [8,10]. The actual in-flight noise, expressed as amplitude spectral density (ASD), is well below the requirement and in the order of

$$\text{ASD}[\delta\nu_R](f) \approx 10^{-15}/\sqrt{f} \cdot 2\nu_R \approx 0.6\text{ Hz}/\sqrt{f} \quad (1)$$

at frequencies above 200 mHz [1,11], where it is dominant and directly apparent in the measured signal due to the lack of other signals at such high frequencies. Assessing the frequency stability at lower frequencies is difficult due to the dominant ranging signal arising from gravitational and non-gravitational differential forces acting on the satellites (cf. black trace in fig. 2, page 9).

On the reference unit, the laser light is split at the beamsplitter into a local oscillator (LO) part and into the transmit (TX) beam (cf. fig. 1). The Triple Mirror Assembly (TMA) routes the TX beam around cold-gas tanks (not shown), towards the distant spacecraft. The emitted frequency is Doppler-shifted when received on the transponder due to the relative motion of the two spacecraft. The Doppler shift ν_D is in the order of some m/s.

The transponder unit employs a frequency-locked loop with a 10 MHz offset, meaning that the frequency ν_T is tuned with high gain and bandwidth such that the beatnote at the photodetector between the local and received, Doppler-shifted light stays at $f_{\text{off}} = 10\text{ MHz}$. This implies that the transponder laser frequency ν_T is the sum of received Doppler-shifted reference frequency $\nu'_R = \nu_R + \nu_D$ and f_{off} . The purpose of the transponder is to send back amplified laser light to the reference with a well-defined and known optical frequency (and phase). Since the transponder is in $220 \pm 50\text{ km}$ distance, it only receives a fraction of the initially emitted light power (in the order of nanowatts). The light beam travels back to the reference side, interferes again and the beatnote between the (again) Doppler-shifted transponder and local reference frequency $f_R = \nu'_T - \nu_R = 2\nu_D + f_{\text{off}}$ contains the desired ranging information, encoded in the Doppler shift ν_D .

3. LRI Phase Observables

Even though a descriptive picture by means of frequencies was given in the previous section, the LRI actually measures the phase of the interference pattern. We now closely follow the approach by Yan et al. [12] to describe the phase observables in a relativistic framework in order to assess potential relativistic effects on the scale factor. We favor this description in terms of phase since that is invariant in the context of general relativity, i. e., independent of the coordinate system, in contrast to the frequency.

In GRACE-FO data analysis, four coordinate systems are of relevance: the local Lorentz frame of reference and transponder satellites, which have their proper time τ_R and τ_T and the origin at the satellite center-of-mass, respectively, and the geocentric non-rotating coordinate system with coordinate time t usually realized through global positioning system (GPS) time. This quasi-inertial geocentric celestial reference frame (GCRF) is usually used in satellite

gravimetry to perform orbit integration. In contrast, the co-rotating terrestrial reference frame is used to perform the gravity field recovery. Following the description in Ashby [13], we assume that the coordinate time t of the GCRF is realized by clocks on the geoid, in contrast to the geocentric coordinate time (TCG) where clocks far away from Earth are assumed.

The phase of the reference laser (RLAS) in the frame of the reference satellite can be written as

$$\Phi_R(\tau_R'', \text{RLAS}) := \int_0^{\tau_R''} v_R(\tau_R) d\tau_R + \text{const.}, \quad (2)$$

where v_R is the instantaneous laser frequency and τ_R'' indicates the measurement epoch. The absolute value of the phase is neither accessible nor relevant here, which is emphasized by the constant term. The variations in the laser frequency of the reference have been addressed with eq. (1).

If we select a particular event $E = (\tau_R(E), \text{RLAS})$ when light with the phase $\Phi_R(E)$ is produced and emitted at the reference laser, that phase value will propagate towards the transponder satellite. In the local Lorentz frame of the transponder satellite, we define the event $E' = (\tau_T(E'), \text{TPR})$ as the reception at the transponder photoreceiver (TPR). The phase of the beatnote at the TPR is given as the phase difference of both interfering light fields, i. e.

$$\varphi_T(E') = \Phi_T(E') - \Phi_R(E') = f_{\text{off}} \tau_T^{\text{USO}}(E') + \delta_T(E'). \quad (3)$$

That measurement is used as feedback in the transponder control loop (cf. section 2), which means it will follow the phase ramp $f_{\text{off}} \tau_T^{\text{USO}}$. The ramp is defined w. r. t. the local time of the Ultra-Stable Oscillator (USO) τ_T^{USO} , which is an electrical realization of the proper time τ_T that may exhibit noise and errors. As these errors are correctable in post-processing (using the CLK1B data product), we regard the proper time realizations τ_R^{USO} and τ_T^{USO} as error-free in the following. Imperfections in the control loop, e. g., due to the limited gain or bandwidth, may result in phase deviations δ_T . Due to the frame invariance of the phase and the way the events E and E' were defined, one can relate the phase $\Phi_R(E')$ at the transponder detector to the phase on the reference laser, i. e.,

$$\Phi_R(E') = \Phi_R(\tau_R(E), \text{RLAS}) = \Phi_R(E). \quad (4)$$

We note that eqs. (2) and (3) can be used to derive the phase (and frequency) of the transponder laser, which is a function of the reference laser.

The phase value of the transponder laser $\Phi_T(E')$ at the instance of detection was also split at the beamsplitter and will propagate back to the reference satellite. We label the event when this phase is impinging on the reference photoreceiver (RPR) as $E'' = (\tau_R(E''), \text{RPR})$ and the corresponding phase of the beatnote on the reference photoreceiver reads

$$\varphi_R(E'') = \Phi_T(E'') - \Phi_R(E''). \quad (5)$$

The phase of the local oscillator field $\Phi_R(E'')$ was emitted at the reference laser a short time before that, the exact delay is given by the light propagation time $\Delta\tau_R^{[a_{R''} + b_{R''}]}$ for the optical path lengths a_R and b_R in the reference frame (cf. fig. 1). The two primes indicate that these quantities refer to the time when the measurement occurs on the reference side. Thus, we obtain

$$\Phi_R(E'') = \Phi_R(\tau_R(E'') - \Delta\tau_R^{[a_{R''} + b_{R''}]}, \text{RLAS}) \quad (6)$$

The received light on the transponder satellite can be rewritten in terms of the reference laser phase plus a contribution from the transponder frequency-locked loop, i. e.

$$\begin{aligned}\Phi_T(E'') &= \Phi_R(\tau_R(E), \text{RLAS}) \\ &\quad + f_{\text{off}} \tau_T(E') + \delta_T(E')\end{aligned}\quad (7)$$

We derive the relation between the light reception time $\tau_R(E'')$, i. e., the measurement time on reference, and light emission time $\tau_R(E)$ in terms of the light paths a, b and ℓ in fig. 1 as

$$\tau_R(E'') - \tau_R(E) \quad (8)$$

$$= (\tau_R(E'') - \tau_R(E')) + (\tau_R(E') - \tau_R(E)) \quad (9)$$

$$= \Delta\tau_R^{[-b_{T'} + \ell_{T'R''} + b_{R''}]} + \Delta\tau_R^{[a_R + \ell_{RT'} + b_{T'}]} \quad (10)$$

$$= \Delta\tau_R^{[\ell_{RT'} + \ell_{T'R''}]} + \Delta\tau_R^{[a_R + b_{R''}]} \quad (11)$$

The round-trip propagation time for light on the racetrack $\Delta\tau_R^{[\ell_{RT'} + \ell_{T'R''}]}$ as apparent in the local Lorentz frame of the reference satellite contains the ranging information and will be written in a short form as $\Delta\tau_R^{[\text{rt}]}$ later on. Again, the primes indicate roughly when light paths or satellite states are evaluated, e. g., double prime means the measurement time, one prime means approx. $220 \text{ km}/c_0 \approx 0.73 \text{ ms}$ earlier and no prime means 1.46 ms earlier than the measurement epoch. Finally, by using eq. (6) and eq. (7) in eq. (5) and employing the definition for the laser phase (cf. eq. (2)), one obtains with the help of eq. (11)

$$\begin{aligned}\varphi_R(\tau_R'') &= - \int_{\tau_R'' - \Delta\tau_R^{[\text{rt}]} - \Delta\tau_R^{[a_R + b_{R''}]}}^{\tau_R'' - \Delta\tau_R^{[a_R + b_{R''}]}} \nu_R(\tau_R) d\tau_R \\ &\quad + f_{\text{off}} \tau_T(E') + \delta_T(E') + \text{const.}\end{aligned}\quad (12)$$

where the short form $\tau_R'' = \tau_R(E'')$ was used. The first line of eq. (12) illustrates that the phase of the beatnote on the reference satellite φ_R contains the elapsed phase between start and end time given by the lower and upper bound of the integral, respectively. This result is consistent with the expression given in [8], though a constant laser frequency was assumed there.

The light propagation time $\Delta\tau_R^{[b_{R'}]}$ for path length b_R appears in both integral bounds with two primes, i. e., at the same epoch. This means that variations in that path between beamsplitter and photodiode do not cause phase variations due to common-mode rejection because that segment is traversed by both beams. The b_R -terms appear because the phase measurement at the photoreceiver is actually defined at the beamsplitter. However, there is a negligible delay until the information arrives at the detector. Delays appear with larger magnitude also in later stages of data processing, e. g., filter delays, and need to be accounted for in data processing (see [14] for more details).

The terms related to path length a_R in eq. (12) are evaluated at different instances, which are separated by the round-trip delay of approx. 1.46 ms . The phase variations on this path delivering light to the beamsplitter over such short time scales can be safely omitted [8].

The transponder phase measurement is mainly a trivial phase ramp:

$$\varphi_T(\tau_T(t)) = f_{\text{off}} \tau_T(t) + \delta_T(\tau_T(t)). \quad (13)$$

The phase on the reference and transponder satellite, φ_R and φ_T , are reported as piston phase in the GRACE-FO LRI Level-1A data product (LRI1A) [15]. The phase measurements

exhibit sporadic phase jumps (or glitches) when some attitude control thrusters are activated [1,16]. Most of the jumps or steps appear simultaneously up to the light travel time on both satellites and have been accounted for in the mathematical description by the δ_T -term. By fitting a model to the individual phase jump in the transponder phase data, one can subtract the same model amplitudes from reference and transponder phase, but with different delay due to light travel time [1]. We denote these deglitched phase time series as φ_T^{DGL} and φ_R^{DGL} and compute the LRI ranging phase as

$$\varphi_{\text{LRI}}(\tau_R(t)) := \varphi_T^{\text{DGL}}(\tau_T(t - \Delta t_{\text{estim}}^{[\ell_{T'R''}]}) - \varphi_R^{\text{DGL}}(\tau_R(t)) \quad (14)$$

$$\Rightarrow \varphi_{\text{LRI}}(t) = \varphi_T^{\text{DGL}}(t_R - \Delta t_{\text{estim}}^{[\ell_{T'R''}]}) - \varphi_R^{\text{DGL}}(t_R). \quad (15)$$

To form the phase difference described in eq. (14), one has to bring the phase values from LRI1A to the same time-grid by means of interpolation. We recommend to first convert the time tags of the reference τ_R and transponder τ_T into coordinate time (t_R and t_T) by using LLK1B, the datation reports from LHK1A, adding the constant phase delay of the downsampling filter [15], and then interpolate the transponder phase onto the time-grid of the reference, because the transponder measurement exhibits less variations. Further, the (approximate) light travel time from transponder to reference $\Delta t_{\text{estim}}^{[\ell_{T'R''}]}$ is used, which can be computed from the GPS positions of the satellites. Note that by converting the local LRI time τ_R into GPS time t_R , they are not regularly sampled anymore and the resulting phase φ_{LRI} needs to be interpolated to derive the regularly sampled reference time-tags t in coordinate time for the final LRI1B data product. Equation (15) can directly be used in data processing using the LRI1A data product.

However, in order to understand the physical content of the computed ranging phase $\varphi_{\text{LRI}}(t)$, we rewrite eq. (15) using the definitions of eqs. (12) and (13) as

$$\varphi_{\text{LRI}}(t) = \int_{t_R - \Delta t_R^{[\text{rt}]}}^{t_R} \nu_R^G(t'_R) dt'_R + q_R, \quad (16)$$

where q_R denotes an arbitrary and unknown phase bias. Note that the absolute laser frequency ν_R^G in the coordinate frame is used here. The relation between the frequency of the laser source ν_R and the apparent frequency in the Earth-centered GCRF system ν_R^G is

$$\nu_R^G = \nu_R \cdot \frac{d\tau_R}{dt}, \quad (17)$$

though the distinction between those is rather of academic interest as discussed in appendix A, since they deviate just at the parts-per-billion level.

The derivative of eq. (16), which is the phase rate, is given by [17]

$$\frac{d\varphi_{\text{LRI}}(t)}{dt} = \frac{d}{dt} \left(\int_{t - \Delta t^{[\text{rt}]}(t)}^t \nu_R^G(t') dt' + q_R \right) \quad (18)$$

$$= \frac{d\Delta t^{[\text{rt}]}(t)}{dt} \cdot \nu_R^G(t - \Delta t^{[\text{rt}]}(t)) + \nu_R^G(t) - \nu_R^G(t - \Delta t^{[\text{rt}]}(t)). \quad (19)$$

From this expression, the physical contributors to the ranging phase can be seen. The first term contains the desired ranging information, i. e., the round-trip propagation time $\Delta t^{[\text{rt}]}$ multiplied by the laser frequency ν_R^G at the emission event. The latter two terms can be regarded as a phase error due to laser frequency changes between the emission and reception time of the

photon. A handy approximation for a slowly varying laser frequency $\nu(t + \Delta t^{[rt]}) \approx \nu(t)$ in both, coordinate time and proper time, is given by

$$\varphi_{\text{LRI}}(t) \approx \Delta t^{[rt]}(t) \nu_{\text{R}}^{\text{G}}(t) + q_{\text{R}} = \Delta \tau_{\text{R}}^{[rt]}(t) \nu_{\text{R}}(t) + q_{\text{R}}. \quad (20)$$

The equivalence of eq. (20) in proper time and coordinate time follows from the phase-invariance under coordinate transformation in general relativity [18].

4. Relation between Phase and Biased Range

Gravity field recovery for GRACE-like missions, i. e., the conversion of range, accelerometer and orbit observations into gravity field coefficients, is usually based on the biased instantaneous inter-satellite range

$$\rho^{\text{inst}} = |\vec{r}_A(t) - \vec{r}_B(t)| + \text{const.} \quad (21)$$

that one tries to obtain using LRI or KBR measurements. However, due to the finite speed of light and the motion of the satellites during the light travel time, these range measurements yield a non-instantaneous biased range, in the LRI case proportional to the round-trip light travel time in the GCRF $\Delta t^{[rt]}$ or in the reference S/C timeframe $\Delta \tau_{\text{R}}^{[rt]}$.

The conversion between LRI-derived raw, biased range $\rho_{\text{LRI}}^{\text{raw}}$ and instantaneous range is in general given by the light time correction (LTC), i. e.,

$$\rho_{\text{LRI}}^{\text{inst}}(t) = \rho_{\text{LRI}}^{\text{raw}}(t) + \rho_{\text{LRI}}^{\text{LTC}}(t) \quad (22)$$

$$= \frac{c_0 \Delta t^{[rt]}(t)}{2} + c_0 \mathcal{T}_{\text{TWR}}^{\text{G}}(t) \quad (23)$$

$$= \frac{c_0 \Delta \tau_{\text{R}}^{[rt]}(t)}{2} + c_0 \mathcal{T}_{\text{TWR}}(t), \quad (24)$$

where $c_0 \mathcal{T}_{\text{TWR}}^{\text{G}}$ is the common light time correction for the LRI, which is derived from orbit information (GNI1B) and for the GCRF [12]. However, a similar correction $c_0 \mathcal{T}_{\text{TWR}}$ could be derived from orbit information also for the local Lorentz frame of the reference satellite. Here we assume the conventional approach, where the light time correction is based on a range from $\Delta t^{[rt]}$. We further need to rescale the ranging phase φ_{LRI} (cf. eq. (16)) in units of cycles with the estimated wavelength $\lambda_{\text{est}}^{\text{G}} = c_0 / \nu_{\text{R},\text{est}}^{\text{G}}$ as apparent in the GCRF in order to obtain the raw LRI range as [17]

$$\rho_{\text{LRI}}^{\text{raw}}(t) = \frac{c_0}{2} \int_0^t \frac{d\varphi_{\text{LRI}}(t')}{dt'} \frac{1}{\nu_{\text{R}}^{\text{G}}(t' - \Delta t^{[rt]}(t'))} - \left(\frac{\nu_{\text{R}}^{\text{G}}(t')}{\nu_{\text{R}}^{\text{G}}(t' - \Delta t^{[rt]}(t'))} - 1 \right) dt' \quad (25)$$

$$= \frac{c_0}{2} \left(\Delta t^{[rt]}(t) - \Delta t^{[rt]}(0) \right) + \text{errors}. \quad (26)$$

Equation (25) provides the recipe to compute the raw biased range as a function of the coordinate time t , which is available after precise orbit determination. The formula follows directly from the definition of the phase derivative (cf. eq. (19)). Equation (26) in turn provides the physical meaning of $\rho_{\text{LRI}}^{\text{raw}}$ as a time-of-flight measurement, whereby the errors include Tilt-To-Length Coupling (TTL) [19], laser frequency noise [1] and others.

5. Error Coupling Model

We showed in eq. (25) that the inter-satellite biased range can be reconstructed from phase measurements, if the conversion factor given by the absolute frequency $\nu_{\text{R}}^{\text{G}}(t)$ or wavelength $\lambda(t) = c_0 / \nu_{\text{R}}^{\text{G}}(t)$ is known. Here we consider errors in the knowledge of the frequency, given

as the difference between estimated and true frequency $\nu_{R,est}^G(t) - \nu_R^G(t)$, which are expressed as a scale factor

$$\varepsilon_{SCF}(t) = \frac{\nu_{R,est}^G(t) - \nu_R^G(t)}{\nu_R^G(t)} \Leftrightarrow \nu_R^G(t) = \frac{\nu_{R,est}^G(t)}{1 + \varepsilon_{SCF}(t)}. \quad (27)$$

By applying the replacement $\nu_R^G(t) \rightarrow \nu_R^G(t)/(1 + \varepsilon_{SCF}(t))$ to eq. (25), we obtain an expression for the estimated range $\rho_{LRI}^{\text{raw,est}}$. In the following, we compute the error of this estimated range. For better readability, we drop the time dependency of terms that are evaluated at the measurement epoch t' .

$$\begin{aligned} & \rho_{LRI}^{\text{raw,est}}(t) - \rho_{LRI}^{\text{raw}}(t) \\ &= \frac{c_0}{2} \int_0^t \frac{\nu_R^G + \varepsilon_{SCF}(t' - \Delta t^{[rt]}) \cdot \dot{\phi}_{LRI}}{\nu_R^G(t' - \Delta t^{[rt]})} - \frac{(1 + \varepsilon_{SCF}(t' - \Delta t^{[rt]})) \nu_R^G}{(1 + \varepsilon_{SCF}) \nu_R^G(t' - \Delta t^{[rt]})} dt' \end{aligned} \quad (28)$$

$$\approx \frac{c_0}{2} \int_0^t \varepsilon_{SCF}(t' - \Delta t^{[rt]}) \Delta t^{[rt]} - \varepsilon_{SCF}(t' - \Delta t^{[rt]}) + \frac{\nu_R^G \varepsilon_{SCF}}{\nu_R^G(t' - \Delta t^{[rt]})} dt' \quad (29)$$

$$\approx \frac{c_0}{2} \int_0^t \varepsilon_{SCF} \Delta t^{[rt]} + \dot{\varepsilon}_{SCF} \Delta t^{[rt]} - \varepsilon_{SCF} + \frac{\nu_R^G \varepsilon_{SCF}}{\nu_R^G(t' - \Delta t^{[rt]})} dt' \quad (30)$$

$$\approx \varepsilon_{SCF}(t) \cdot \frac{c_0}{2} \Delta t^{[rt]}(t) + \frac{c_0}{2} \int_0^t \varepsilon_{SCF} \left(\frac{\dot{\nu}_R^G}{\nu_R^G} \Delta t^{[rt]} + 1 \right) - \varepsilon_{SCF} dt' \quad (31)$$

$$\approx \varepsilon_{SCF}(t) \cdot L(t) \quad (32)$$

where we used a rigorous approximation to obtain the simple result. The approximation in eq. (29) is based on the relation $1/(1 + \varepsilon_{SCF}) \approx 1 - \varepsilon_{SCF}$ together with the definition of the phase derivative in eq. (19) and we dropped a second order term in ε_{SCF}^2 . Equation (30) uses $\varepsilon_{SCF}(t - \Delta t^{[rt]}) \approx \varepsilon_{SCF}(t) - \Delta t^{[rt]} \dot{\varepsilon}_{SCF}(t)$ and neglects product terms of $\Delta t^{[rt]} \cdot \Delta t^{[rt]}$. The result of eq. (31) employed the same type of approximations, namely $1/\nu_R^G(t' - \Delta t^{[rt]}) \approx (1 + \dot{\nu}_R^G / \nu_R^G \cdot \Delta t^{[rt]}) / \nu_R^G$. In order to solve the integral, we omitted product terms of $\dot{\nu}_R^G / \nu_R^G$ with ε_{SCF} or $\dot{\varepsilon}_{SCF}$, because these describe a second order cross-coupling between scale error and fractional true frequency change that is expected to be negligible. $L(t) = c_0 \Delta t^{[rt]}(t) / 2$ denotes the absolute distance between the spacecraft and the error coupling $\varepsilon_{SCF}(t) \cdot L(t)$ resembles the well-known influence of (fractional) laser frequency variations into the range measurement [8], which can be regarded as a scale factor error.

The second error contributor that we address is a potential timeshift ζ of the measured LRI data, arising from unconsidered internal delays of the LRI. At startup, the LRI time is initiated via the Onboard Computer (OBC), which introduces a delay of 1.5 s at maximum [15], although we only observed values below 1.0 s. In order to compensate this delay, the differences of LRI time and MWI Instrument Processing Unit (IPU) time is measured regularly (called the datation report) and is used to correct the LRI time tags. However, a small deviation ζ may remain, even after this subtraction. We linearize the effect of this potential timeshift to first order as

$$\rho_{LRI}^{\text{inst}}(t + \zeta) \approx \rho_{LRI}^{\text{inst}}(t) + \zeta \cdot \dot{\rho}(t), \quad (33)$$

where we use the approximate range rate $\dot{\rho} \approx \dot{\rho}_{LRI}^{\text{raw}} \approx \dot{\rho}_{LRI}^{\text{inst}}$ for terms that describe a small error coupling and where the highest precision in $\dot{\rho}$ is not required.

Figure 2 illustrates the significance of the static scale factor error $\varepsilon_{SCF} = 10^{-6}$ (green) and timeshift $\zeta = 50 \mu\text{s}$ (red). The effects of these are exceeding or are close to the LRI noise requirement for frequencies between 0.6...3 mHz, indicating that the scale factor and timeshift

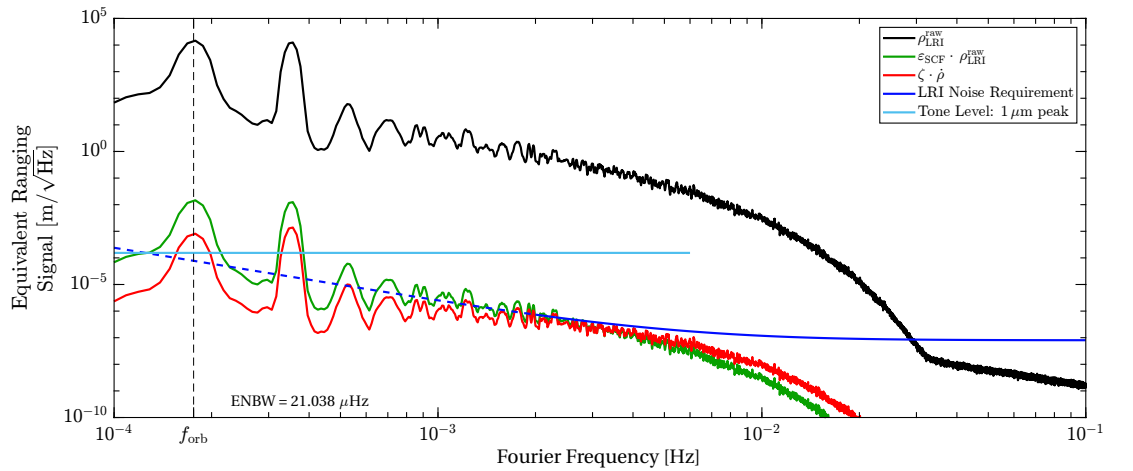


Figure 2. Typical amplitude spectral density of the LRI ranging signal (black) and effective errors arising from a static scale factor error $\varepsilon_{\text{SCF}} = 10^{-6}$ (green) and timeshift $\zeta = 50 \mu\text{s}$ (cf. eq. (33)). Also shown is the noise requirement of LRI (blue), which is strictly applicable only for frequencies above 2 mHz, but it was extrapolated towards lower frequencies (blue dashed segment). The light blue line denotes a 1 μm tone amplitude. The ranging measurement is dominated by laser frequency noise at highest frequencies (above 30 mHz), and by the differential gravitational and non-gravitational forces below.

needs to be known to better precision, e. g., at the level of 10^{-7} to 10^{-8} for the scale and at a level of a few microsecond or better for the timeshift. Fourier frequencies below 0.6 mHz are dominated by sinusoidal errors at integer multiples of the orbital frequency $f_{\text{orb}} \approx 0.18 \text{ mHz}$. These peaks need to be compared to tone error requirements with the unit of meter (rms or peak) instead of spectral densities with the unit of $\text{m}/\sqrt{\text{Hz}}$. An indicative level for tone errors is 1 μm (peak), which is a requirement for the MWI at 2/rev frequency in GRACE-FO [20], is shown in light blue. The shown errors exceed the one micron tone level as well by approximately two orders of magnitude.

By combining the effects due to a scale factor error (eq. (32)) and an uncompensated timeshift (eq. (33)), we obtain the error of the LRI measured range w.r.t. the truth as

$$\rho_{\text{LRI}}^{\text{inst}}(t) - \rho_{\text{true}}^{\text{inst}}(t) \approx \varepsilon_{\text{SCF}}(t) \cdot L(t) + \zeta \cdot \dot{\rho}(t) . \quad (34)$$

6. Scale Factor Determination

The scale factor ε_{SCF} provides an estimate $\nu_{\text{R,est}}$ for the actual laser frequency ν_{R} of the LRI reference unit, which in turn is needed for accurately converting the phase measurement into a range in meter. Here we present three different approaches to either calculate the absolute laser frequency ν_{R} directly, or through the scale factor ε_{SCF} , that is related to absolute laser frequency through eq. (27).

Since GRACE-FO hosts the KBR and LRI, the obvious way to obtain the LRI scale ε_{SCF} (or frequency ν_{R}) is to compare the ranging data of the two instruments. We define the instantaneous KBR range as

$$\rho_{\text{KBR}}^{\text{inst}}(t) = \rho_{\text{KBR}}^{\text{raw}}(t) + \rho_{\text{KBR}}^{\text{LTC}}(t) + \rho_{\text{KBR}}^{\text{AOC}}(t) . \quad (35)$$

The three quantities on the right-hand side are the ionosphere-free K/Ka band range $\rho_{\text{KBR}}^{\text{raw}}$, the KBR Light Time Correction (LTC) and the antenna offset correction (AOC), cf. [15], which are regarded as error-free. They are given in the KBR1B data product [15]. Ultimately, daily arcs of

LRI phase measurements can be calibrated against the KBR ranging data, i. e., by minimizing the KBR-LRI residuals as

$$\left\| \rho_{\text{KBR}}^{\text{inst}}(t) - \lambda_{\text{est}}^{\text{SDS}} \cdot \varphi_{\text{LRI}}(t + \zeta) - \rho_{\text{LRI}}^{\text{LTC}} \right\| \rightarrow 0 \quad (36)$$

using a daily constant laser wavelength $\lambda_{\text{est}}^{\text{SDS}}$ and timeshift ζ as fit parameters. The KBR scale factor error can be regarded as negligible, since the relevant USO frequency is determined during precise orbit determination. The USO fractional frequency varies by about 10^{-11} , mainly at 1/rev [17, Fig. 1], and we assume the knowledge error to be even smaller. The processing of daily chunks of data essentially decomposes the scale factor ε_{SCF} into a static and time-variable part as

$$\varepsilon_{\text{SCF}}(t) = \langle \varepsilon_{\text{SCF}} \rangle + \delta \varepsilon_{\text{SCF}}(t), \quad (37)$$

of which only the static part $\langle \varepsilon_{\text{SCF}} \rangle$ is determined.

This cross-calibration scheme is the official processing strategy employed by the Science Data System (SDS) for the LRI1B data product in version 04, where a conversion factor from phase to range and a timeshift ζ is estimated once per day. The scale $\langle \varepsilon_{\text{SCF}}^{\text{SDS}} \rangle$ is reported in the ionospheric correction (`iono_corr`) column of the LRI1B files, whereas the timeshift ζ is applied through LLK1B. The scale value relates to the laser frequency and wavelength estimates through

$$\lambda_{\text{est}}^{\text{SDS}}(t_{\text{daily}}) = (1 + \langle \varepsilon_{\text{SCF}}^{\text{SDS}} \rangle(t_{\text{daily}})) \cdot \lambda_0 \quad (38)$$

and

$$\nu_{\text{est}}^{\text{SDS}}(t_{\text{daily}}) = \frac{\nu_0}{\left(1 + \langle \varepsilon_{\text{SCF}}^{\text{SDS}} \rangle(t_{\text{daily}})\right)}, \quad (39)$$

where ν_0 is a nominal frequency for the LRI lasers, given in the documentation as $\nu_0 = 281\,616\,393$ MHz and $\nu_0 = 281\,615\,684$ MHz for GF-1 and GF-2, respectively [15]. The two nominal values were determined pre-flight, but do not represent the best knowledge of the actual frequency. The corresponding nominal wavelength is $\lambda_0 = c_0/\nu_0$. Equation (39) is in principle a reformulation of eqs. (27) and (37), however, the time-varying part $\delta \varepsilon_{\text{SCF}}(t)$ is neglected by the processing of daily segments. Therefore, eq. (25) simplifies to

$$\rho_{\text{LRI}}^{\text{SDS}}(t) = \frac{c_0}{2} \frac{(1 + \langle \varepsilon_{\text{SCF}}^{\text{SDS}} \rangle)}{\nu_0} \cdot \varphi_{\text{LRI}}(t). \quad (40)$$

The minimization result for $\langle \varepsilon_{\text{SCF}}^{\text{SDS}} \rangle$ as given in the LRI1B-v04 data product is shown in green in fig. 3. Our recomputation with an in-house Level 1A to 1B processing is denoted as $\langle \varepsilon_{\text{SCF}}^{\text{AEI}} \rangle$ (blue) and this will be used later on as one possible frequency model. The plot covers the timespan from 2018-Dec-13 until 2022-Jan-01, where GF-1 acts as the LRI reference unit throughout the whole period. The LRI was not in science mode from 2019-Feb-06 to 2019-Mar-17 due to spacecraft related outages. Smaller gaps in the data originate from phase breaks, e. g., due to spacecraft maneuvers or diagnostic data recording. The frequent data gaps starting in mid 2021 are due to nadir-pointing of the spacecraft, occurring roughly on two days per week. In these periods, the pointing angles between the spacecraft-fixed coordinate system and the line-of-sight exceed the LRI pointing capabilities.

Even though the blue and green traces match, the SDS implementation seems to be less robust as it shows more outliers, which may be related to imperfect phasejump removal [1]. The amount of outliers reduces after 2020-Jun-27, when the deglitching algorithm was adjusted

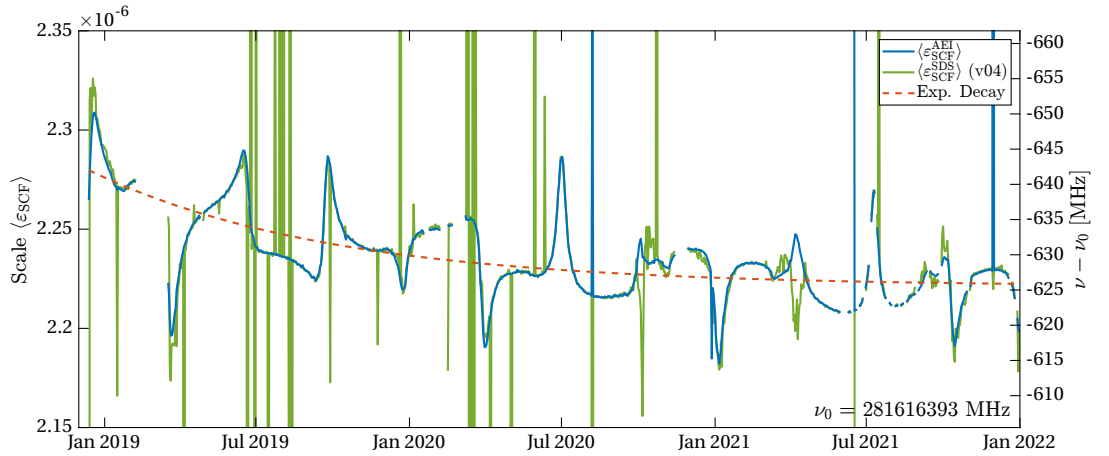


Figure 3. Comparison of LRI scale factor $\langle \varepsilon_{\text{SCF}} \rangle$ using the conventional cross-calibration method. *Blue:* using the AEI ranging phase φ_{LRI} , cf. eq. (25). *Green:* the SDS LRI1B-v04 result. *Orange dashed:* Exponential model for the cavity resonance frequency. The right axis shows the equivalent laser frequency variations (cf. eq. (39)).

by the SDS [21]. Both traces show a slow drift that seems to converge and peaks and dips occurring roughly every three month, indicating an apparent change of the laser frequency with a magnitude of $\pm 10^{-7}$ or ± 20 MHz. It is noteworthy that we can not distinguish, which instrument contributes to those periodic variations, as we always use the difference between LRI and KBR. However, the variations will be addressed in more detail in sections 10 and 11. The slow drift in fig. 3 was fitted as exponential decay of the form

$$\varepsilon^{\text{Cav}}(t) = \varepsilon_{\infty}^{\text{Cav}} - \varepsilon_0^{\text{Cav}} \exp(-\lambda^{\text{Cav}} \cdot t) \quad (41)$$

and is shown in orange. The decay rate is $\lambda^{\text{Cav}} = 4.006 \times 10^{-8} / \text{s}$, with $\varepsilon_{\infty}^{\text{Cav}} = 2.221 \times 10^{-6}$ and $\varepsilon_0^{\text{Cav}} = -1.190 \times 10^{-7}$, the time t is GPS seconds past 2018-May-22 at midnight. Exponential shrinkage (and thus increasing frequency) has already been observed in similar cavities made from ultra-low expansion (ULE) materials and the suspected cause is aging of the spacer material [22]. Equation (41) can of course be converted into an equivalent frequency model ν_R^{Cav} via eq. (39). This exponential model is the second model for the laser frequency, resulting in similar values as the SDS scheme, but without the periodic features. Until now, we only derived these exponential model coefficients for GF-1, the derivation for GF-2 is beyond the scope of this manuscript

The scheme of cross-calibration is only possible due to the unique situation of having two independent ranging measurements by KBR and LRI. However, it can not resolve intraday frequency variations of the LRI and introduces small discontinuities at day-bounds. Furthermore, it depends on the KBR, which likely won't be present in future missions. Therefore, we present an on-ground calibration, that has been performed for the two laser flight models as a third method to determine the laser frequency, and derive a calibrated frequency model only using telemetry data of the LRI. It is based on the fact, that the laser frequency ν_R can be deduced from the setpoints of the frequency-lock control loop and thermal state of the laser. With this model, we can in principle evaluate the optical frequency in orbit continuously with moderate accuracy. The laser frequency may change due to varying environmental conditions, e. g., temperatures of the optical reference cavity. This particular model will be derived in sections 7 to 9. All models are analyzed and compared to each other in section 10.

7. LRI Laser and Telemetry Description

The LRI Reference Laser Units (RLUs) were built by Tesat Spacecom and are comparable to the laser onboard LISA Pathfinder and to the LISA baseline [23]. They are based on a Nd:YAG non-planar ring oscillator (NPRO) crystal and are fiber-connected to an optical reference cavity built by Ball Aerospace [10,24] and to the Optical Bench Assembly (OBA). The laser's output power is in the order of 25 mW in the near infrared regime [25]. The laser frequency is actively controlled by feedback control loops using the PDH scheme [9] to lock the laser to the reference cavity (in reference mode) or to the incoming beam using a frequency-offset lock (transponder mode). The tuning is achieved through a thermal element for slow variations and a Piezo-Electric Transducer (PZT) actuator for fast variations. The actuator signals are downlinked in the laser telemetry and published within the LHK1A/B data products at a rate of 1 Hz, if the LRI is in science mode, i. e., when the laser link is established. The data type is unsigned integer of 32 bits depth. The corresponding normalized signed data streams are computed via the two's complement and a scaling by the bit depth as

$$u2i(x, N) = \begin{cases} x/2^N - 1, & \text{if } x > 2^{N-1} \\ x/2^N, & \text{if } x \leq 2^{N-1} \end{cases} \quad (42)$$

with $N = 32$ and x denoting the unsigned value from the telemetry. The value range is $-1/2 < u2i(x, \cdot) \leq 1/2$. These normalized data streams are denoted as pztIL, pztOOL, thermIL and thermOOL in the following. The temperature of the laser can be retrieved from OFFRED data, which is recorded by the OBC. The measurement is taken at the Thermal Reference Point (TRP) of the RLU, which is located at the housing of the laser itself. By the time of writing, the laser TRP temperature is not publicly available, but it will be shown later that the influence of the TRP coupling is small during nominal operations.

The notations in-loop (IL) and out-of-loop (OOL) are not referring to different sensors as in conventional feedback control circuits, but two parts that are added to form the final setpoint. The OOL channel is used for manual control with some logic (e. g., to drive a frequency ramp for locking to the cavity or during acquisition), whereas the IL value represents the evolution of the actuator value in closed-loop operation. The actuator range of the PZT and thermal actuators is ± 1 V and ± 9 V, respectively, with nominal frequency coupling coefficients of 5 MHz/V and 500 MHz/V, respectively.

8. RLU On-Ground Calibration

The laboratory setup to calibrate the LRI lasers is shown in fig. 4. It consisted of the LRI flight laser, the Laser Ranging Processor (LRP) (including the phasemeter), a frequency-controlled reference laser and a wavemeter. During these activities, the frequency of the reference laser is tuned via the computer and its frequency is recorded using a wavemeter. The LRI unit in transponder mode locks its laser frequency to the incoming beam and adds a 10 MHz offset and is thus known as well. During the activities, the RLU temperature as well as the PZT and thermal telemetry is recorded. The frequency of the LRI laser was not measured directly, since it was more convenient to use the second output port of the reference laser (one fiber to the wavemeter, one to the optical bench), while the LRI laser light is free-beam on the optical bench. We apply a linear model for the on-ground (OG) laser frequency estimate:

$$v^{OG}(t) = \begin{pmatrix} c_{pztIL} \\ c_{pztOOL} \\ c_{thermIL} \\ c_{thermOOL} \\ c_{lasTRP} \end{pmatrix} \cdot \begin{pmatrix} pztIL(t) \\ pztOOL(t) \\ thermIL(t) \\ thermOOL(t) \\ lasTRP(t - \tau) - 26^\circ C \end{pmatrix} + v_{0,air} + \Delta v_{AirToVac}, \quad (43)$$

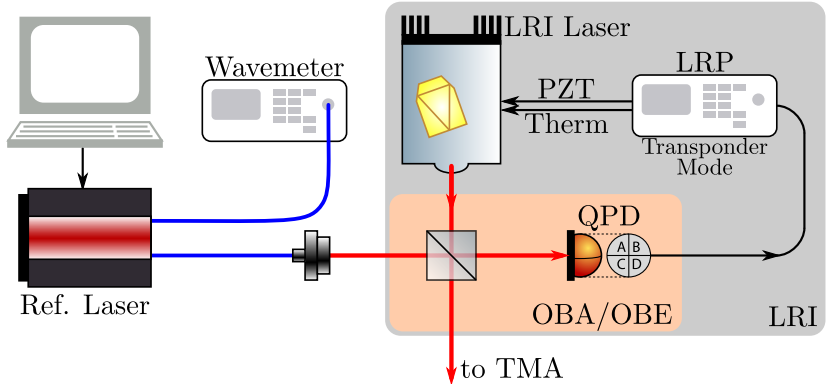


Figure 4. Laboratory setup for the LRI flight laser frequency calibration measurement. Blue lines denote optical fibers, red lines are laser beams in free space. Black arrows denote electric signals.

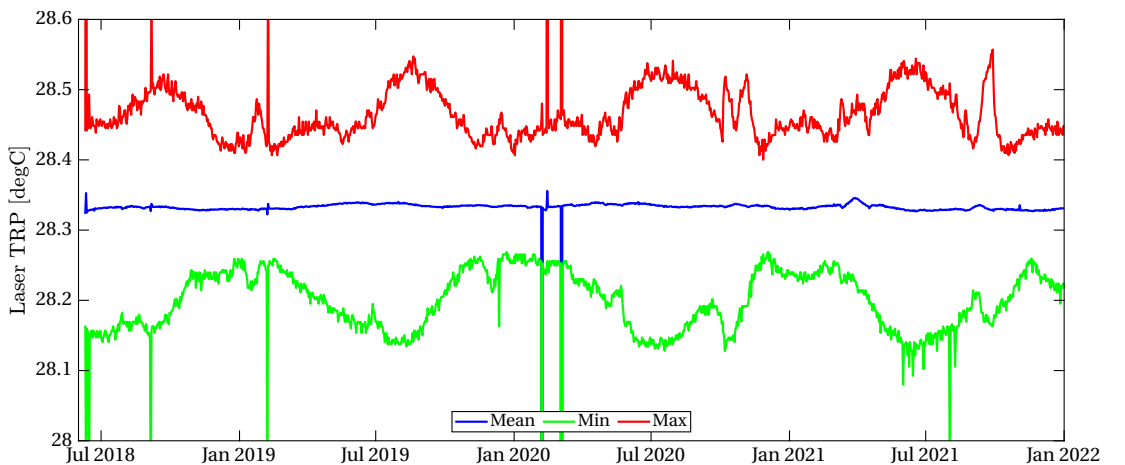


Figure 5. Daily mean, min and max of the GF-1 1asTRP data.

which depends on the actuator states, i. e., the telemetry data streams `pztIL`, `pzt00L`, `thermIL`, `therm00L` as well as the surrounding temperature, which is measured at the TRP of the laser. Since the TRP is located outside the thermal shielding, a time delay of $\tau = 520$ s is applied to the temperature measurements, which represents the travel time of outer temperature changes to the NPRO crystal. Furthermore, only deviations from the nominal temperature of 26 °C are considered.

The nominal values for the coupling factors as given by the laser manufacturer are shown in table 1. However, we refine the thermal coupling coefficients for the individual laser units with our own measurements. The PZT and TRP coupling are not refined, since they were not modulated strong enough during the calibration measurements for deriving reliable coupling factors. We expect the TRP coupling to be non-critical, since the lasers' TRP temperature varies only in the sub-Kelvin domain in flight as shown in fig. 5. The blue trace depicts the daily averaged laser TRP recording of GF-1 together with its respective daily minimum (green) and maximum (red) value. Apparently, the temperature of the GF-1 laser is stable when averaged on a daily basis and shows sub-daily variations of ± 0.2 K, which translates into $\Delta\nu = \pm 2.4$ MHz in frequency, or $\varepsilon_{\text{SCF}} \approx \Delta\nu/\nu \approx \pm 8.5 \times 10^{-9}$ using a coupling of -12 MHz/K (cf. table 1).

Several calibration measurements were performed on both RLUs between July 2017 and January 2018. For the laser integrated in GF-2, four measurements were taken. In the following, we label these four measurements (1)...(4). They all differ a little in their procedure. In (1) the reference laser's frequency was commanded in discrete steps, which caused the LRP to

Table 1. Coupling factors for the two LRI laser flight units. Shown are the design values provided by the laser manufacturer and fit results from on-ground measurements. PZT and TRP coupling factors were not refined, since the measurements were not suitable to derive these couplings. The static value $\Delta\nu_{\text{AirToVac}}$ was provided by the manufacturer and represents the frequency change from air to vacuum.

Coupling	Unit	Design value	GF-1 (fit)	GF-2 (fit)
c_{pztIL}	[MHz]	$2 \text{ V} \cdot 5 \text{ MHz/V} = 10 \text{ MHz}$	-	-
c_{pztOOL}	[MHz]	$18 \text{ V} \cdot 5 \text{ MHz/V} = 90 \text{ MHz}$	-	-
c_{thermIL}	[MHz]	$2 \text{ V} \cdot 500 \text{ MHz/V} = 1000 \text{ MHz}$	1097	1094
c_{thermOOL}	[MHz]	$18 \text{ V} \cdot 500 \text{ MHz/V} = 9000 \text{ MHz}$	9155	8857
c_{lasTRP}	[MHz/K]	-12	-	-
ν_0, air	[MHz]	281 614 803 (GF-1) 281 614 780 (GF-2)	281 614 682.081	281 614 631.999
$\Delta\nu_{\text{AirToVac}}$	[MHz]	37 (GF-1) 27 (GF-2)	-	-

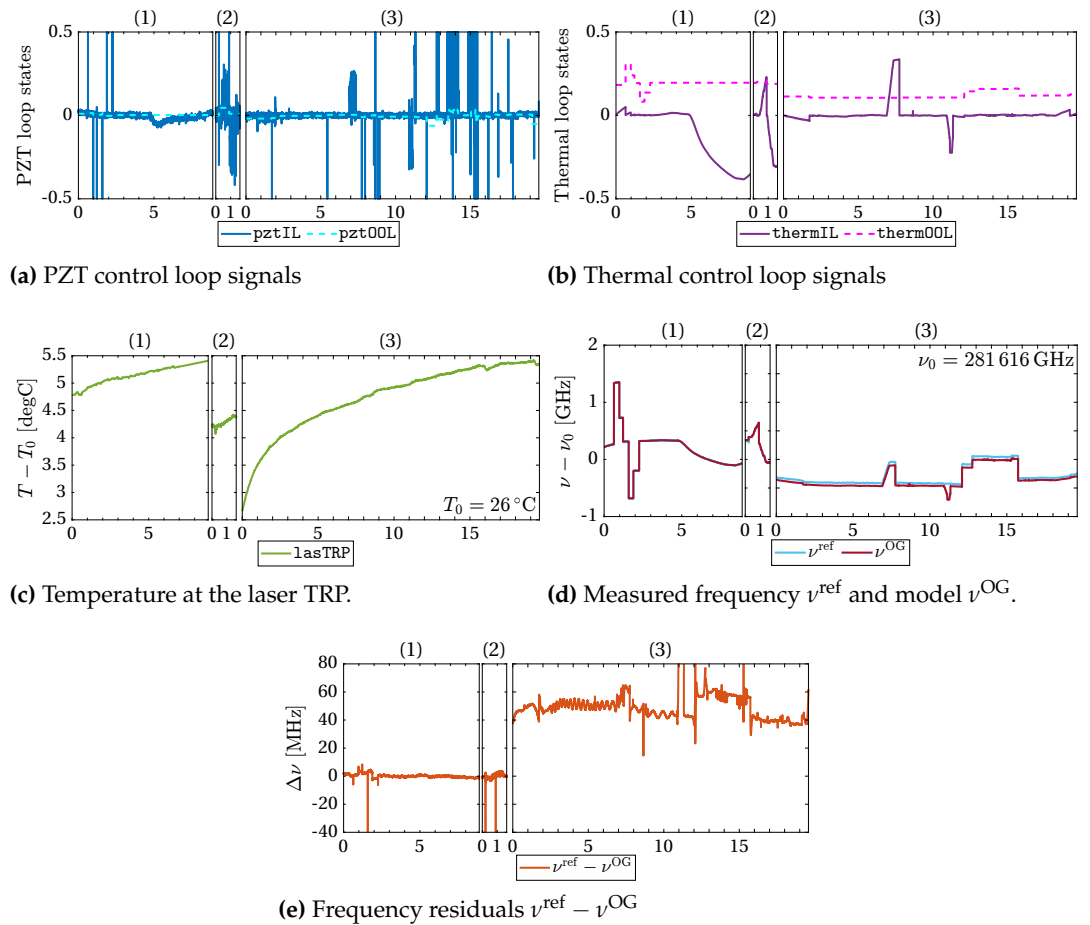


Figure 6. Regression results for the GF-2 laser. The numbering on top of the individual panels of each subfigure corresponds to the measurement campaigns, as explained in the text. Note the offset in the residuals in (e) when the less precise wavemeter WS6-600 was used in campaign (3). The average bias here is 51.494 MHz. All x-axes are in arbitrary time units.

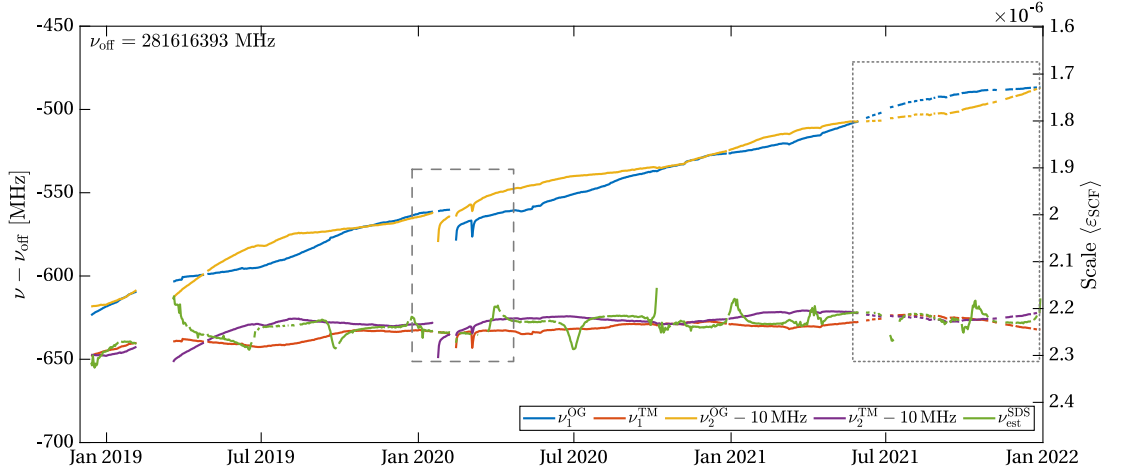


Figure 7. Purely ground calibration-based models $\nu_{1/2}^{\text{OG}}$ and empirically corrected Telemetry (TM) models $\nu_{1/2}^{\text{TM}}$ for GF-1 and GF-2 laser frequencies alongside the SDS frequency $\nu_{\text{est}}^{\text{SDS}}$ from KBR-LRI cross-calibration. Outliers in SDS curve removed. The right axis shows approximate equivalent laser frequency variations, cf. eq. (39).

lose lock and forced a reacquisition and thus a short data loss. Afterwards, the reference laser was put into a free-running cool down mode without active stabilization. Reacquisition was avoided in (2) by sweeping continuously over the same frequency range. (3) was a diagnostic test for the Differential Wavefront Sensing (DWS) and the absolute frequency measurement was a secondary result. Test (4) consists of very few sample points only, since the used wavemeter had no digital output port but only a display to retrieve the data. Thus, the data of (4) is not used in this analysis. The measurements (1) and (2) were performed in July 2017 using a HighFinesse WS7-60 wavemeter with an absolute accuracy of 60 MHz. Test (3) in November 2017 used a HighFinesse WS6-600 (600 MHz accuracy) and in (4), a Burleigh WA1500 (60 MHz accuracy) was used. The GF-1 laser, was tested twice: once with a WS6-600 in November 2017 and a Burleigh WA1500 in January 2018 and again, the latter one is not used in this analysis.

We use a least squares approach to estimate the linear coupling factors and constants of eq. (43). Additionally, we weight the WS7-60 measurements higher by a factor of 5 compared to the WS6-600, which has lower accuracy. We furthermore estimate a relative offset of the WS6-600 wavemeter, which we can deduce by analyzing the residuals. This offset of the WS6-600 is also apparent when measuring an absolute frequency reference like an iodine cell, see appendices B and C for more information.

Figure 6 shows the result of the regression using the measurements for GF-2. The individual measurement campaigns are labeled (1)...(3). The subfigures (a) and (b) show the normalized telemetry of the laser control loops, the temperature of the laser's TRP is shown in subfigure (c). Panel (d) contains the absolute frequency of the reference laser ν^{ref} (shifted by 10 MHz to compensate for the offset-frequency lock of the LRP) and the resulting laser frequency model ν^{OG} of the LRI laser. The trace in (e) shows the residuals $\nu^{\text{ref}} - \nu^{\text{OG}}$, which clearly shows an offset of approximately 50 MHz beginning at (3), where the WS6-600 was used. The high-frequency variations are higher in (3) due to the lower precision of the WS6-600. The resulting coupling factors from the linear least squares minimization are shown in table 1. In general, the resulting values match the manufacturers design values with only slight deviations.

9. Empirical Refinement of Telemetry-Based Laser Frequency Model

The calibrated OG frequency models $\nu_{1/2}^{\text{OG}}$ based on laser telemetry are now compared to the frequency $\nu_{\text{est}}^{\text{SDS}}$ (cf. eq. (39)) from the KBR-LRI cross-correlation, where the flight data spanning from 2018-Dec-13 until 2022-Jan-01 is used. Figure 7 shows the frequency estimates from the OG models for both spacecraft (blue and yellow) alongside the SDS frequency (green). The latter one is actually already shown in fig. 3, but outliers are removed now. The GF-2 curves are shifted down by 10 MHz to remove the intended transponder frequency offset (cf. section 2). The subscript 1/2 refers to GF-1 or GF-2, respectively.

The OG models (blue and yellow) differ by 20 MHz at maximum, which is within the accuracy of the better wavemeter WS7-60, defining the model accuracy. However, a drift of the models w.r.t. the KBR cross-calibration method (green) is visible. The current hypothesis for this drift is an aging effect of the NPRO crystal or of the electronics within the LRP. However, there is little literature on aging-induced frequency changes of NPRO lasers, and this theory might need verification in a laboratory experiment. The drift appears only in the laser setpoint telemetry, but not in the frequency, which is tightly locked to the cavity resonance.

The curves show some data gaps starting mid 2021, which are caused by regular nadir-pointing periods, in which the LRI was not creating science data (dotted box in fig. 7). The steep slopes and the dip in February and March 2020 in $\nu_{1/2}^{\text{OG}}$ (dashed box) are due to spacecraft-related non-science phases of the LRI, after which the units had to heat up to reach the nominal temperatures. This heating process is visible at the laser TRP (cf. fig. 5) and thus affects not only the OG model but also the green SDS curve with comparable magnitude, which confirms the temperature coupling estimate in the OG model. However, we found that the link acquisition happened before the lasers reached their thermal equilibrium, which caused an apparent small step in the $\nu_{1/2}^{\text{OG}}$ frequency model (see appendix D). This could eventually be caused by imperfect coupling factors. To account for these steps ν_i^{step} in our telemetry-based laser frequency model, as well as for the drifts a and offsets $\Delta\nu$ from the NPRO aging, we define an empirical correction and estimate its parameters by least squares minimization using $\nu_{\text{est}}^{\text{SDS}}$ as the reference. The empirical model reads

$$\nu^{\text{emp}}(t) = a \cdot (t - t_0) + \Delta\nu + \nu^{\text{step}}(t), \quad (44)$$

where the reference epoch $t_0 = 1210982400$ GPS is 2018-May-22 at midnight. The steps are defined as

$$\nu^{\text{step}}(t) = \nu_i^{\text{step}} \text{ if } t_i^{\text{step}} \leq t < t_{i+1}^{\text{step}}. \quad (45)$$

The estimated parameters a and $\Delta\nu$ are shown in table 2a, while the steps ν_i^{step} and the corresponding time-tags t_i^{step} are shown in table 2b. Unfortunately, this empirical model makes the telemetry-based frequency model still dependent on the KBR. In principle, one could overcome the needs of an empirical model by better calibrating the laser prior to launch. This empirical model is subtracted from the on-ground model to form the final telemetry-based (TM-based) frequency estimate

$$\nu_{1/2}^{\text{TM}}(t) = \nu_{1/2}^{\text{OG}}(t) - \nu_{1/2}^{\text{emp}}(t). \quad (46)$$

After applying the empirical model, the numerical values of the full frequency models $\nu_{1/2}^{\text{TM}}$ for GF-1 and GF-2 (orange and purple traces in fig. 7) are in the range of $\nu_{\text{est}}^{\text{SDS}}$. Other than the cross-calibration method, the telemetry-based model does not show seasonal or periodic features. Note, that the exponential drift of the cavity is contained in $\nu_{\text{est}}^{\text{SDS}}$ and $\nu_{1/2}^{\text{TM}}$, even though it is hard to see in the fig. 7. However, the empirical model in eq. (44) does not absorb

Table 2. Parameters for the empirical part of the laser frequency model for GF-1 and GF-2 of eq. (44).

(a) Drift Parameters			(b) Steps in the telemetry-based laser frequency model. Time tags refer to midnight.		
Coupling	Unit	Value	i	t_i^{step}	$\nu_i^{\text{step}} [\text{MHz}]$
		GF-1		GF-1	GF-2
a	[Hz/s]	1.419	1	2018-05-22	0
$\Delta\nu$	[MHz]	-5.881	2	2020-01-10	0
		1.110	3	2020-02-10	-11.593
		-1.089	4	2020-05-11	-10.446
			5	2022-01-01	2.881
					2.881
					undefined
					undefined

the effect of exponentially increasing frequency (cf. fig. 3 and eq. (41)), since that cavity drift is present in both, ν_1^{TM} and the reference $\nu_{\text{est}}^{\text{SDS}}$, thus it is not apparent in the metric of the least squares adjustment.

10. Comparison of the LRI1B-Equivalent Data Sets

We now derive alternative in-house LRI1B-equivalent ranging data [17,26] by employing eq. (25). In total, three versions are computed, which differ by the models for the laser frequency ν_R^G . At first, the data product using the telemetry-based model as described in the previous section (cf. eq. (46)) is called LRI1B-v51. The exponential cavity model (cf. eq. (41)) is used to form LRI1B-v52. The last data product, LRI1B-v53, uses the predetermined, constant value ν_0 only, which makes it in principle a pre-release of LRI1B-v04 without the scale $\langle \varepsilon_{\text{SCF}}^{\text{SDS}} \rangle$ and timeshift ζ applied. The further differences of all three version to the official v04 data are the improved deglitching algorithm [26] and the LTC implementation according to [12]. The LRI ranging data for these three versions at a 10 Hz data rate is derived for the time spanning from 2018-Dec-13 until 2022-Jan-01.

For all three data products, we compute scale $\langle \varepsilon_{\text{SCF}} \rangle$ and timeshift ζ by cross-correlation KBR and LRI again (similar to eq. (36)) and determine the impact on KBR-LRI residuals in terms of variations in $\langle \varepsilon_{\text{SCF}} \rangle$ and ζ . This time however, we include the correction term for KBR frequency variations $\rho_{\text{KBR}}^{\text{FV}}$ as proposed by [17]. Note that a similar correction is already included in $\rho_{\text{LRI}}^{\text{inst}}$ through eq. (25). Hence, we define the error range

$$\rho_{\text{err}}(t) = \rho_{\text{LRI}}^{\text{inst}}(t) - \rho_{\text{KBR}}^{\text{inst}}(t) - \rho_{\text{KBR}}^{\text{FV}}(t) \quad (47)$$

$$= \langle \varepsilon_{\text{SCF}} \rangle \cdot \rho_{\text{LRI}}^{\text{inst}}(t) + \zeta \cdot \dot{\rho}(t) + \delta \rho_{\text{LRI-KBR}}(t), \quad (48)$$

where the first line is a modified form of eq. (34), referenced to the KBR range instead of the unknown true range. The second line shows that the error range can be decomposed into a part that is consistent with a daily constant scale factor error $\langle \varepsilon_{\text{SCF}} \rangle$, a part that is caused by a daily-constant delay ζ and remaining residuals described by $\delta \rho_{\text{KBR-LRI}}$, which can, for instance, absorb changes in the scale factor $\delta \varepsilon_{\text{SCF}}(t)$ (cf. eq. (37)). Furthermore, we use the instantaneous, biased LRI range $\rho_{\text{LRI}}^{\text{inst}}(t)$ instead of the absolute distance $L(t)$, since their difference is only a constant bias, which is neglected anyway in interferometric measurements.

Since we observe drifts in the order of a few 10 $\mu\text{m}/\text{day}$ in the KBR-LRI residuals below the orbital frequency, we apply a high pass FIR filter with a cutoff frequency of $0.08 \text{ mHz} \approx f_{\text{orb}}/2$ to the error range ρ_{err} . This filter is not affecting the signals at 1/rev or higher frequency, which have the main impact on the LRI scale factor according to our assessment. Future studies may

also address the reason for the long-term drifts, but this is beyond the scope of this study. The filtered error range is denoted as

$$\tilde{\rho}_{\text{err}} = \text{HPF}(\rho_{\text{err}}, 0.08 \text{ mHz}) . \quad (49)$$

Half a day of data is cropped at the start and end of each continuous segment, i. e., at every loss of the interferometric link of either KBR or LRI, to remove the initialization of the FIR filter, hence all data gaps appear longer than they actually are. Clearly, $\tilde{\rho}_{\text{err}}$ contains errors of both ranging instruments.

After minimizing the error range $\|\tilde{\rho}_{\text{err}}\| \rightarrow 0$ on daily arcs, the static values for scale $\langle \varepsilon_{\text{SCF}} \rangle$ and timeshift ζ as well as the rms residuals if $\delta\rho_{\text{KBR-LRI}}$ are used as metrics to assess the mismatch between KBR and LRI. The estimated parameters are not meant to be applied as a correction. The discussion of the $\delta\rho_{\text{LRI-KBR}}(t)$ -term is postponed to the next section. The results for all three LRI1B products are shown as the blue curves in fig. 8. The left and right columns of subplots show the scale $\langle \varepsilon_{\text{SCF}} \rangle$ and timeshift ζ , respectively, while the three data products v51, v52 and v53 are shown in the different rows. For visual representation, the blue curve of fig. 8e was shifted by 2.23×10^{-6} and all blue traces in the right column are shifted by a $75 \mu\text{s}$ offset.

Using the nominal frequency ν_0 yields the need for a large scale factor of $\langle \varepsilon_{\text{SCF}} \rangle(v53) \approx 2.2 \times 10^{-6}$ (blue curve in fig. 8e) with seasonal variations in the order of 5×10^{-8} . It is in principle the same curve as $\nu_{\text{est}}^{\text{SDS}}$ of fig. 7, which again confirms the validity of our processing. The telemetry based frequency model (v51) already reduces the numerical values of the scale factor to approximately $\langle \varepsilon_{\text{SCF}} \rangle(v51) \approx \pm 5 \times 10^{-8}$, since the model values ν_1^{TM} are closer to the true laser frequency than the nominal value ν_0 . The exponential cavity model (v52) performs similar to v51. The timeshift ζ , that is needed to match the KBR and LRI data the best, varies between 50 and 100 μs in all three cases (cf. right column). This timeshift would ideally be zero, however this delay is introduced at an unknown stage in the timing architecture (see appendix E for a brief discussion of the LRI time frame). None of the three absolute frequency models is capable to reduce the seasonal plateaus, peaks, and dips in both, scale and timeshift, which correspond to tone errors with a magnitude of roughly $30 \mu\text{m}$ at $1/\text{rev}$ ¹ in either of the two ranging instruments. Our hypothesis is that these features are driven by errors at $1/\text{rev}$ and $2/\text{rev}$ frequencies, which we address in the next section.

11. Thermal Correction of LRI Ranging Data

Changes in the thermal environment at many units on the spacecraft are predominantly appearing at $1/\text{rev}$ and $2/\text{rev}$ frequencies and may alter the measured range. We identified two possible coupling mechanisms. First, the coupling could be in the frequency regime, like temperature changes of the cavity acting as an additional scaling term. Second, errors could occur in the phase regime, e. g., due to temperature-dependent alignment of components or temperature-driven effects in the electronics. We call these two corrections the Thermal Correction (TC). In this section we model the two possible effects and estimate linear coupling factors, with units of $1/\text{K}$ and m/K , in order to further minimize the residuals between LRI and KBR.

The error range (cf. eqs. (48) and (49)) is computed for the time from 2018-Dec-13 until 2022-Jan-01, where the LRI on GF-1 acts as reference, and downsampled from 10 Hz to 1/300 Hz for decreasing computational costs. All computations explained in the following are performed independently for LRI1B-v51, v52 and v53 and are compared against KBR1B-v04. Initially, the KBR-LRI residuals show rms variations of $24.852 \mu\text{m}$, $24.828 \mu\text{m}$ and $664 \mu\text{m}$, respectively, and

¹ Assuming a $1/\text{rev}$ ranging signal of $\rho = 600 \text{ m}$ and scale factor variations of $\delta\varepsilon_{\text{SCF}} = 5 \times 10^{-8}$, we obtain $\langle \varepsilon_{\text{SCF}} \rangle \cdot \rho = 30 \mu\text{m}$.

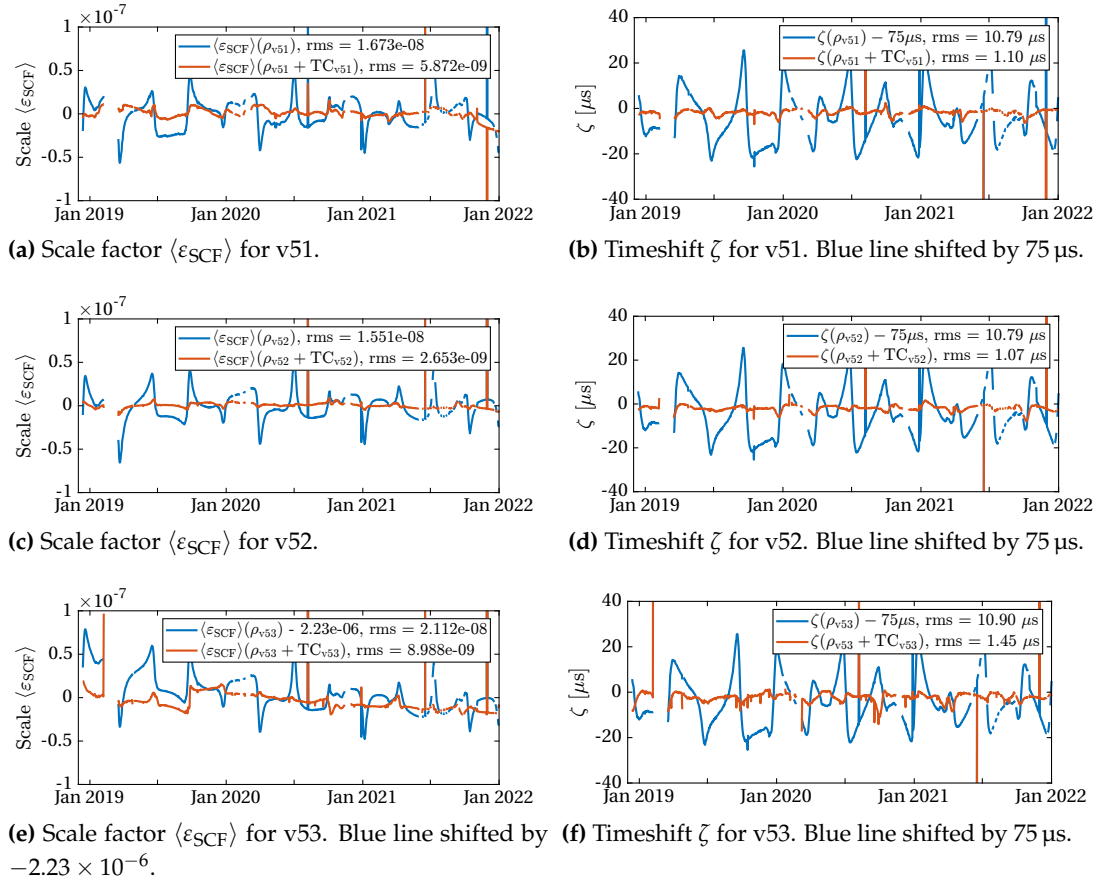
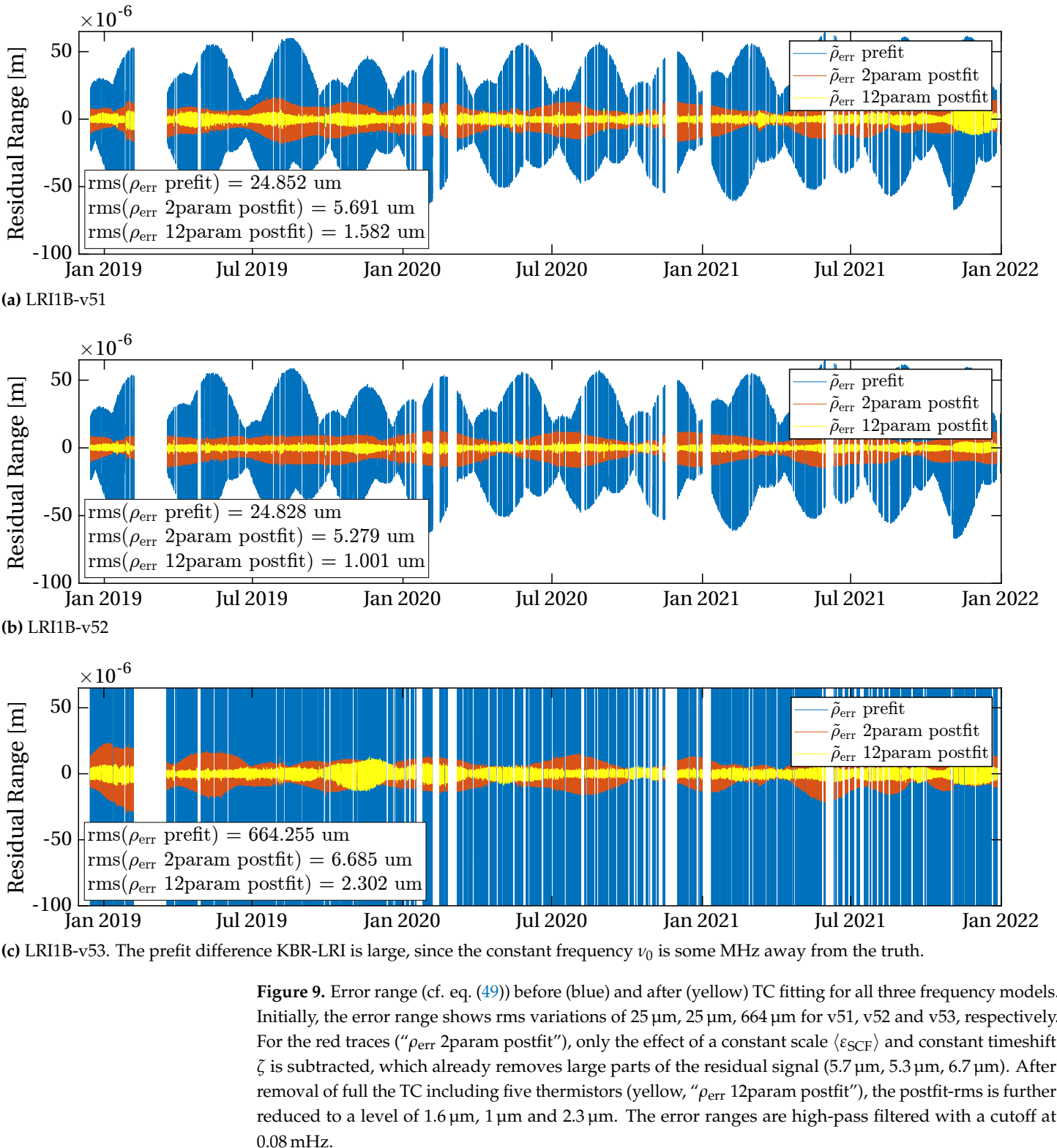


Figure 8. Comparison of scale and timeshift for LRI1B-v51, v52 and v53. Each subplot shows the results from the raw data product (blue) and including the Thermal Correction (TC) in red. Left column: Scale factor $\langle \varepsilon_{SCF} \rangle$ for different frequency models v51, v52, v53. Right column: corresponding timeshift ζ . From top to bottom: v51, v52, v53. Outliers removed for computing the rms values.

are shown as blue traces in the subplots of fig. 9. The top panel shows v51, the middle panel v52 and the third panel v53. The error range $\tilde{\rho}_{err}$ of all three cases shows prominent 1/rev oscillations (apparent as a broadening of the traces), whose magnitude varies on large (seasonal) time scales. The huge residuals for v53 are expected, since the nominal frequency ν_0 are some MHz from the actual laser frequency.

In a first step, we numerically a single estimate for the constant parameters scale $\langle \varepsilon_{SCF} \rangle$ and time bias ζ of eq. (48) for the whole span of almost four years, which remove most of the residual KBR-LRI deviations. This implies that we do no longer interpret eq. (48) on a daily basis only. This intermediate result (yellow curves in fig. 9) reduces the rms residuals to $5.691 \mu m$, $5.279 \mu m$ and $6.685 \mu m$, respectively. However, this level is still above the KBR measurement noise of $0.4 \mu m^2$, which we expect to limit our comparison.

² We assume a $10 \mu m / \sqrt{Hz}$ white noise in the KBR with 1/300 Hz sampling rate. This yields $10 \mu m / \sqrt{Hz} / 2/300 \approx 0.4 \mu m$ rms.



Afterwards, we aim to describe the residual variations $\delta\tilde{\rho}_{\text{KBR-LRI}}$ from eq. (48), which effectively describe the variations in the scale factor and timeshift, using

$$\tilde{\rho}_{\text{TC}}(t) := \sum_i \delta\tilde{\rho}_{\text{KBR-LRI},i}^{\text{freq}}(t) + \sum_i \delta\tilde{\rho}_{\text{KBR-LRI},i}^{\text{phase}}(t), \quad (50)$$

where we account for two different error coupling mechanisms. In case of the frequency-domain coupling, we define

$$\delta\tilde{\rho}_{\text{KBR-LRI},i}^{\text{freq}}(t) = \text{HPF}(L(t) \cdot (c_1 \cdot T_i(t) + c_2 \cdot \dot{T}_i(t)), 0.08 \text{ mHz}). \quad (51)$$

The different temperature sensors onboard the spacecraft are denoted as $T_i(t)$. Importantly, we use a temperature coupling proportional to the absolute range $L = 220 \pm 50 \text{ km}$ to account for the full effect from the roundtrip propagation, similarly to eq. (32). The coefficients c_1 and c_2 have units of $1/\text{K}$ and s/K , respectively. They can be converted to approximate equivalent laser frequency couplings in units of Hz by multiplying with $\nu_0 \approx 281 \text{ THz}$. The second term $c_2 \cdot \dot{T}$ originates from a potential timeshift due to propagation time from temperature changes to the measurement and is linearized to first order. This timeshift can be computed by $\zeta_T = c_2/c_1$. It should be noted, that a positive sign of ζ_T is not violating causality, since the timeshift can always be regarded as a modulus of the orbital frequency. The cm-precision of the GPS-based absolute range L (e. g. using GN11B-v04) is sufficient.

The phase-domain equation reads

$$\delta\tilde{\rho}_{\text{KBR-LRI},i}^{\text{phase}}(t) = \text{HPF}(c_1 \cdot T_i(t) + c_2 \cdot \dot{T}_i(t), 0.08 \text{ mHz}), \quad (52)$$

where the coefficients have the units m/K and $\text{s} \cdot \text{m}/\text{K}$, respectively. The high-pass filter removes frequencies below 1 CPR, i. e., long-term drifts, but maintains 1 CPR which has high relevance for the scale factor. We introduce $T_{\text{AC/DC},i}$ as the ensemble of all temperature sensors on both spacecraft (161 per SC, retrieved from so-called OFFRED data and downsampled to 1/300 Hz as well), which are decomposed into high- and low-frequency parts by filtering using the same cutoff frequency of 0.08 mHz as for the error range. We expect, that the DC-parts are more likely to cause variations in frequency regime ($1/\text{K}$), while the AC-parts cause m/K -couplings. This is due to the fact, that the DC-part likely contains a large static offset with only slight variations, which would imply a constant offset in $\tilde{\rho}_{\text{err}}$ if the phase-domain coupling would apply, but large 1/rev tones in case of the frequency coupling due to the coupling multiplication with L in eq. (51).

An optimization algorithm iteratively picks a single temperature sensor that minimizes $\tilde{\rho}_{\text{err}}$ the most. To do so, the parameters c_1 and c_2 from eqs. (51) and (52) are determined for both components $T_{\text{AC},i}$ and $T_{\text{DC},i}$ of each temperature sensor T_i in every iteration and the minimization gain, i. e., the residual rms of KBR-LRI *with* this particular correction term divided by the residual rms *without*, is computed. For every iteration, the parameters of all the previously added sensor as well as $\langle \varepsilon_{\text{SCF}} \rangle$ and ζ are always co-estimated alongside the new sensor, hence we extend the design matrix for the least squares minimization by two columns per iteration.

The algorithm stops after adding 5 sensors, giving 12 coefficients in total: two global scale $\langle \varepsilon_{\text{SCF}} \rangle$ and timeshift ζ biases for the whole time span (corresponding to the first two terms in eq. (48)) and two coefficients for each selected temperature sensor according to eqs. (50) to (52). The estimated constants for scale and timeshift are shown in table 3, whereas the corresponding thermistor coefficients are shown in tables 4a to 4c for the ranging products v51, v52 and v53, respectively. The resulting error ranges are also shown in fig. 9, once for applying only the correction of the scale and timeshift (orange, “ $\tilde{\rho}_{\text{err}}$ 2param postfit”) and once for the full model

Table 3. Global scale factor $\langle \epsilon_{\text{SCF}} \rangle$ and timeshift ζ for the data span from 2018-Dec-13 to 2022-Jan-01 determined by the Thermal Correction fit.

LRI1B version	$\langle \epsilon_{\text{SCF}} \rangle$	ζ
v51	-1.626×10^{-8}	$67.81 \mu\text{s}$
v52	-3.810×10^{-9}	$67.95 \mu\text{s}$
v53	2.387×10^{-6}	$68.40 \mu\text{s}$

including the temperature couplings (yellow, “ $\tilde{\rho}_{\text{err}} \text{ 12param postfit}$ ”). The subtraction of the full TC model is capable of reducing the KBR-LRI rms residuals to a level of $1.6 \mu\text{m}$ (v51), $1.0 \mu\text{m}$ (v52) and $2.3 \mu\text{m}$ (v53).

We observe that in the first iteration, a sensor called “SaMz**” was chosen in all three cases, which is attached to the zenith-pointing (minus z solar array). We expect, that the underlying satellite interior’s thermal environment is highly correlated to this sensor, since the solar arrays are directly heated by the sun and thus exhibit large temperatures variations. Other interesting findings are the LRI OBA and laser temperatures appearing in the coefficients for v52, but none of the models uses a thermistor attached to the cavity. We highlight, that most of the temperature sensors inside the spacecraft are highly correlated. There might be other sets of five sensors, that could produce very similar results.

For verifying the TC, the daily scale and timeshift of KBR and LRI, but now adding $\tilde{\rho}_{\text{TC}}(t)$ to $\rho_{\text{LRI}}^{\text{inst}}$, are computed again, as done in section 10. The new residual scale and timeshift of the LRI range including TC are shown in orange in fig. 8. They clearly show less seasonal variations compared to the blue curves without TC. The best performance, by means of reducing the variations in the scale factor $\langle \epsilon_{\text{SCF}} \rangle$ in the KBR-LRI differences, is achieved when using v52 (utilizing the exponential cavity frequency model) in combination with the TC. Here, the rms variations of the scale factor $\langle \epsilon_{\text{SCF}} \rangle(\rho_{\text{v52}})$ are reduced from 1.551×10^{-8} to 2.653×10^{-9} . Also, the corresponding timeshift $\zeta(\rho_{\text{v52}} + T\zeta_{\text{v52}})$ performs best, with rms variations of about $1 \mu\text{s}$ when including the TC correction $\tilde{\rho}_{\text{TC}}$.

We emphasize, that the TC parameters shown in table 4 can also be used to correct the LRI1B-v04 dataset by SDS, however one has to revert the effects of the daily $\langle \epsilon_{\text{SCF}}^{\text{SDS}} \rangle$ and ζ beforehand, which are already applied in Level 1B³.

12. Discussion

The goal of the methods presented in this paper is to derive an independent and reliable model for the absolute laser frequency ν_R of the LRI lasers in-flight. With this, we try to minimize the dependency of the LRI on the KBR instrument, which is used in nominal processing by the SDS for estimating the scale factor (and thus the frequency). However, in a future mission, there will likely be LRI-like ranging instrument only which requires a new processing scheme. For these missions, there are several options for determining the absolute laser frequency.

The ground-calibrated models $\nu_{1/2}^{\text{OG}}$ as described throughout this manuscript are not accurate enough for gravity field recovery, as their uncertainty (even if we include the empirical correction) is limited by the accuracy of the wavemeter, that was used to determine the coupling coefficients. In the case of the LRI, the accuracy is limited at $60 \text{ MHz} \approx 0.2 \text{ ppm}$. However, with proper calibration procedures on ground, including the drifts of the laser and the cavity, such a model could serve as a backup solution. The same holds for determination of the scale

³ Note, that ζ is already applied in LRI1B, it can be extracted by forming the difference of the time offsets (`eps_time`) provided in CLK1B and LLK1B.

Table 4. Temperature coupling parameters. The index i denotes the order of importance, i. e., the gain in reducing the rms residuals. The frequency range f denotes AC or DC temperature components and $\delta\tilde{\rho}$ type denotes the coupling in phase or frequency regime. Thus, the unit of c_1 is m/K, if f equals AC and 1/K, if f equals DC. The coefficient c_2 has units s m/K (AC) or s/K (DC). The last column $\zeta_T = c_2/c_1$ describes the timeshift of the temperature data in seconds. Positive values do not harm causality, since this timeshift is always a modulus of the orbital period $1/f_{\text{orb}} \approx 5600$ s.

(a) v51

i	SC	Sensor ID	Readable Name	f	$\delta\tilde{\rho}$ type	c_1	c_2	ζ_T [s]
1	GF-1	THT10013	SaMzPx	AC	phase	-1.127×10^{-7}	-6.240×10^{-6}	55.4
2	GF-2	THT10133	BatTrp	AC	phase	-1.173×10^{-5}	-1.379×10^{-3}	117.6
3	GF-1	THT10144	Pr21	DC	freq	-1.642×10^{-9}	-1.501×10^{-6}	914.0
4	GF-1	THT10022	LriLpcMy	DC	freq	2.640×10^{-9}	1.182×10^{-6}	447.9
5	GF-1	THT10143	Oct11	AC	phase	4.153×10^{-6}	-9.814×10^{-4}	-236.3

(b) v52

i	SC	Sensor ID	Readable Name	f	$\delta\tilde{\rho}$ type	c_1	c_2	ζ_T [s]
1	GF-1	THT10013	SaMzPx	AC	phase	-1.302×10^{-7}	6.194×10^{-6}	-47.6
2	GF-2	THT10138	MepFrontPy	AC	phase	-2.238×10^{-7}	5.403×10^{-5}	-241.4
3	GF-1	THT10007	GpsOccAnt	DC	freq	1.513×10^{-11}	-2.382×10^{-8}	-1573.9
4	GF-2	THT10089	LriOba	AC	phase	-1.080×10^{-5}	1.091×10^{-3}	-101.0
5	GF-2	THT10113	LriLas	DC	freq	1.049×10^{-10}	-1.121×10^{-6}	-10689.7

(c) v53

i	SC	Sensor ID	Readable Name	f	$\delta\tilde{\rho}$ type	c_1	c_2	ζ_T [s]
1	GF-2	THT10032	SaMzMx	AC	phase	-1.022×10^{-7}	1.923×10^{-5}	-188.2
2	GF-2	THT10052	AccPanel	DC	freq	-9.162×10^{-9}	-4.827×10^{-6}	526.8
3	GF-2	THT10138	MepFrontPy	AC	phase	-4.996×10^{-6}	8.787×10^{-4}	-175.9
4	GF-2	THT10157	Oct22	DC	freq	5.288×10^{-10}	3.349×10^{-7}	633.4
5	GF-2	THT10052	AccPanel	AC	phase	8.433×10^{-5}	-3.014×10^{-3}	-35.7

factor during gravity field recovery, where preliminary studies showed, that the precision is in the range of 0.2 ppm as well.

A well known and broadly used technique is iodine spectroscopy, where the hyperfine transition line of an iodine molecule is used as absolute reference for a laser lock [27]. This has also been done in the course of calibrating the LRI RLU (cf. appendices B and C) and there are aims to build flight-ready hardware, see e. g. [28]. Optionally, there is the possibility for a hybrid lock to both, an optical cavity and an iodine reference, for having the advantage of a high-frequency stability using a conventional PDH lock as well as the absolute readout using the iodine. The achievable accuracy for such hybrid locks is in the order of $\delta\nu/\nu \approx 10^{-13}$ or $30\text{Hz}/\sqrt{\text{Hz}}$ above 1 mHz with a $1/f$ increase towards lower frequencies [29]. However, the drawback of the saturated doppler-free spectroscopy technique is the need for high optical powers in the order of some hundred mW.

Another technique is to extend the existing PDH lock by adding a sideband at the approximate cavity free spectral range (FSR) (usually some GHz) with imprinted upper and

lower sidebands (some MHz) to the conventional PDH modulation signal before the phase modulator. This enables the readout of the actual cavity FSR w. r. t. the tone frequency (and thus the generating USO frequency), similarly as the usual PDH error signal. After determination of the USO frequency during precise orbit determination, this technique is able to provide an estimate for the FSR frequency with high accuracy. The principle has been demonstrated in laboratory experiments with an accuracy of roughly $3\text{ MHz} \approx 1\text{ ppb}$ [30,31]. The advantage of this technique is that the changes in existing flight-hardware are only minor.

13. Conclusion

In this paper, the methodology to derive a precise range from raw interferometric phase measurements was introduced and applied to in-flight data of the GRACE-FO LRI instrument. With these equations we show that the LRI measured phase is to first order proportional to the product of roundtrip light travel time $\Delta t^{[\text{rt}]}$ and the laser frequency ν_R^G of the reference laser. We further address the conversion from phase to range through the laser frequency in an integral form. The theoretical part of this paper is concluded with the derivation of the two dominant error terms, namely a time-variable scaling of the laser frequency, expressed through a scale factor ε_{SCF} , and a timeshift ζ of the LRI measurement w. r. t. the reference measurement given by the KBR. Importantly, variations in ε_{SCF} couple into the range proportionally to the absolute distance L between the two satellites.

In the second part, we presented three different models to determine the laser frequency in-flight, which are to large extend independent of KBR measurements, once the model values are determined. Based on these models, we derive three versions of the in-house LRI1B-equivalent data product, namely v51, v52 and v53. The first method (v53) uses a constant, nominal laser frequency ν_0 , which was determined prior to launch, but does not represent the best knowledge of the in-flight truth. Thus, v53 is in principle a pre-release for the official LRI1B-v04 by SDS, where a cross-calibration between LRI and KBR ranging data is applied additionally to determine the variations of the scale factor ε_{SCF} . This approach is limited to a single scale factor value per day. The scale factor as determined from the cross-calibration revealed a settling effect of the resonance frequency of the optical reference cavity, which was reported before in literature for ULE cavities. We use this exponential function (cf. eq. (41)) to form v52. For v51, a laser frequency model that can be derived by using LRI data solely, was introduced. By calibrating the laser frequency actuators on ground before launch, one can relate the control loop setpoints of the laser with the resulting frequency. The setup of the pre-flight calibration measurements is explained and the calibration factors are shown. This simple OG-model was then applied to four years of in-flight data of the GRACE-FO mission. It was found, that the model frequency (or more precisely, the setpoints of the laser control loops) seems to drift over time by roughly 40 MHz/yr , and furthermore two steps were observed when the lasers were operated in non-nominal conditions. The physical reason for the drift and steps remains unknown, but they can be compensated by a linear empirical model. We emphasize that the measurements taken pre-flight were never meant to derive a laser frequency model with the highest accuracy. However, with more thorough calibration procedures, one could potentially derive a telemetry model that already accounts for a drift for future missions. Other differences of all three data sets from the official v04 are the deglitching algorithm and the LTC.

Afterwards we focused on analyzing variations of the KBR-LRI residuals, which we call the error range ρ_{err} , by decomposing the error range in contributions of a static scale factor $\langle \varepsilon_{\text{SCF}} \rangle$, a timeshift ζ and the remainder. We observed, that all data sets still show the seasonal variations in scale and timeshift, which were first observed for the cross-calibration scheme, and thus none of the three laser frequency models was capable of removing them.

The last part of this paper discussed a Thermal Correction (TC), where we assumed temperature related errors in the range measurement of either LRI or KBR. We accounted for two coupling mechanisms, one in phase domain and one in frequency domain. An algorithm to determine the coupling factors for all temperature sensors on both spacecraft was explained and equations to compute the TC were given. The minimization in the algorithm is based on the error coupling model derived in the theoretical part. For each of the three datasets, a TC composed of 12 coupling factors (which includes five temperature sensors) was derived. For each temperature sensor we derived a linear coupling c_1 and a potential time delay $\zeta_T = c_2/c_1$ through first order series expansion. Furthermore, two global parameters for the scale $\langle \epsilon_{SCF} \rangle$ and timeshift ζ were determined. We denote, that it is unclear whether the LRI or KBR instrument is responsible for the residual variations of $\tilde{\rho}_{err}$. We showed, that the differential rms variations between LRI and KBR can be reduced from approx. $25 \mu\text{m}$ to $1 \mu\text{m}$ when using LRI1B-v52 including the TC. At this level, the approach is probably limited by the KBR noise.

One big advantage of the frequency models and the TC derived in this paper is that it does no longer rely on the KBR instrument after deriving the coupling coefficients. Thus, the telemetry based model (v51) could be used even without a KBR, e.g., if the KBR (or IPU) on GF-2 breaks.

Author Contributions: Conceptualization, Malte Misfeldt and Vitali Müller; Funding acquisition, Gerhard Heinzel; Investigation, Malte Misfeldt, Vitali Müller, Laura Müller and Henry Wegener; Project administration, Gerhard Heinzel; Writing – original draft, Malte Misfeldt; Writing – review & editing, Vitali Müller, Laura Müller, Henry Wegener and Gerhard Heinzel.

Funding: This work has been supported by: The Deutsche Forschungsgemeinschaft (DFG, German Research Foundation, Project-ID 434617780, SFB 1464); Clusters of Excellence “QuantumFrontiers: Light and Matter at the Quantum Frontier: Foundations and Applications in Metrology” (EXC-2123, project number: 390837967); the European Space Agency in the framework of Next Generation Geodesy Mission development and ESA’s third-party mission support for GRACE-FO; the Chinese Academy of Sciences (CAS) and the Max Planck Society (MPG) in the framework of the LEGACY cooperation on low-frequency gravitational-wave astronomy (M.IFA.QOP18098).

Data Availability Statement: GRACE-Follow On Level-1 instrument data is distributed by the GRACE/GRACE-FO project via NASA PODAAC (<https://podaac-tools.jpl.nasa.gov/drive/files/allData/gracefo>). Other data described throughout the manuscript can be made available upon request.

Acknowledgments: The authors would like to thank the JPL LRI team for helpful regular discussions and insights.

Conflicts of Interest: The authors declare no conflict of interest.

Abbreviations

The following abbreviations are used in this manuscript:

ASD	amplitude spectral density	LRI	Laser Ranging Interferometer
DWS	Differential Wavefront Sensing	LRP	Laser Ranging Processor
FSR	free spectral range	LTC	Light Time Correction
GCRF	geocentric celestial reference frame	MCM	Mass Change Mission
GPS	global positioning system	MTS	modulation transfer spectroscopy
GRACE	Gravity Recovery And Climate Experiment	MWI	Microwave Instrument
GRACE-FO	GRACE Follow-On	NGGM	Next Generation Gravity Mission
IL	in-loop	NPRO	non-planar ring oscillator
IPU	MWI Instrument Processing Unit	OBA	Optical Bench Assembly
KBR	K-band Ranging	OBC	Onboard Computer
		OG	on-ground

OGSE Optical Ground Support Equipment	TM Telemetry
OOL out-of-loop	TMA Triple Mirror Assembly
PDH Pound-Drever-Hall	TPR transponder photoreceiver
PZT Piezo-Electric Transducer	TRP Thermal Reference Point
RLAS reference laser	TTL Tilt-To-Length Coupling
RLU Reference Laser Unit	ULE ultra-low expansion
SDS Science Data System	USO Ultra-Stable Oscillator
TC Thermal Correction	

Appendix A. Distinction of ν_R and ν_R^G

In the main text we stated, that the differences between the optical frequency in the local Lorentz frame of the spacecraft and in the GCRF frame are small. Here, we assess the magnitude of the dominant DC and 1/rev errors. Equation (17) defined, that

$$\nu_R^G = \nu_R \cdot \frac{d\tau}{dt} . \quad (A1)$$

We evaluate the error we introduced by assuming $d\tau/dt = 1$ in Earths gravitational potential. We assume $v = 7.7 \text{ km/s}$, $GM = 3.986 \times 10^{14} \text{ m}^3/\text{s}^2$ and $r = (6378 + 490) \text{ km}$ for the GRACE Follow-On (GRACE-FO) orbit. The fractional clock error at DC frequency is given by [14, eq. 2.14]

$$\frac{d\tau}{dt} - 1 \approx -\frac{v^2}{2c_0^2} - \frac{GM}{r c_0^2} \approx -1 \times 10^{-9} . \quad (A2)$$

This numerical value is far below the 1 ppm requirement given in section 4 and translates in a DC frequency difference of

$$\frac{\nu_R^G}{\nu_R} = \frac{d\tau}{dt} \Rightarrow \nu_R^G - \nu_R \approx 300 \text{ kHz} . \quad (A3)$$

From GNI1B orbit data, one can furthermore infer that the variations of $d\tau/dt$ are below 10^{-11} at the orbital frequency [17], giving a 1 CPR uncertainty of approximately

$$\nu_R^G - \nu_R \approx 3 \text{ kHz} \cos(2\pi f_{\text{orb}}) , \quad (A4)$$

which is again well below the precision goal.

Appendix B. Calibration of WS6-600 using Iodine Cell

Various measurement campaigns for determining the on-ground (OG) frequency models for the two laser flight models of the Laser Ranging Interferometer (LRI) have been performed in the time between July 2017 and January 2018. Over these campaigns, three different wavelength meters (or wavemeters) have been used: A WS6-600 and a WS7-60 by HighFinesse / Angstrom and a WA1500 by Burleigh. The first one has an absolute accuracy of 600 MHz, while the latter two are more accurate by one order of magnitude. The two HighFinesse devices were used mostly during the testing campaigns. They have a built-in calibration via a neon lamp. To verify this internal calibration, the reference frequency of a well known iodine hyperfine transition was used. Iodine is a commonly used molecule for stabilizing lasers to an absolute frequency reference, see e.g. [27,32].

At first, the accuracy of the WS6-600 was measured in a setup consisting of the OGSE laser (Optical Ground Support Equipment), a Prometheus laser by Coherenct, Inc. [33] with a noise eater providing 500 mW output power at a wavelength of 1064 nm. The secondary output provides 20 mW of frequency-doubled light at 532 nm. The laser is internally intensity

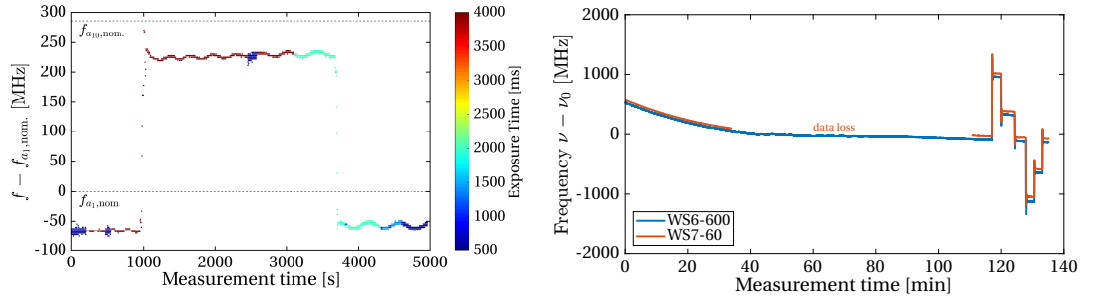


Figure A1. Absolute frequency measurements of the reference laser locked to different hyperfine lines of an iodine cell. The apparent quantization of approximately 3 MHz arises from the finite resolution of 10^{-5} nm of the wavemeter WS6-600. Outliers removed. The small oscillations are observed repeatedly for this wavemeter. The color indicates the wavemeter's exposure time.

Figure A2. OGSE laser frequency, measured with two wavemeters. 110 min waiting for thermal equilibrium, afterwards active control using the laser's thermal elements. Outliers removed. $\nu_0 = 281\,616\,307$ MHz.

stabilized via a noise eater. The frequency of this reference laser can be tuned over a range of roughly 60 GHz via thermal elements and piezoelectric transducers [33].

The OGSE laser's frequency is locked via Doppler-free modulation transfer spectroscopy (MTS) to the R(56)32-0 iodine line, of which we used the a_1 and a_{10} components. The iodine cell was manufactured by InnoLight as well. The nominal frequency of the a_{10} hyperfine component is [34]

$$\nu_{a_{10}} = 563\,260\,223.513 \text{ MHz} . \quad (\text{A5})$$

The a_{10} component's frequency is elevated by $\delta\nu_{\text{vis}} = 572.1$ MHz w. r. t. the a_1 component [27]. Hence,

$$\nu_{a_1} = \nu_{a_{10}} - \delta\nu_{\text{vis}} = 563\,259\,651.413 \text{ MHz} . \quad (\text{A6})$$

The corresponding difference frequency at 1064 nm is

$$\delta\nu_{\text{IR}} = 286.05 \text{ MHz} , \quad (\text{A7})$$

which we ideally will measure in our test setup. Our first calibration measurement, shown in fig. A1, took 5000 s, of which the laser was locked to the a_1 component in the beginning and in the end for approximately 1000 s and to the a_{10} component in between. The optical power in the fiber going to the WS6-600 was relatively low at about 850 nW. The average frequency measured for ν_{a_1} at 1064 nm is about 60 MHz below the nominal value, which is within the 600 MHz accuracy of the device. The measured frequency difference between the two hyperfine components a_1 and a_{10} is $\delta\nu_{\text{meas.}} = 288.785$ MHz, being 2.735 MHz higher than $\delta\nu_{\text{IR}}$. Other measurements confirmed a bias of this device by approximately 20 to 60 MHz, while the relative measurements are more precise. The small oscillations with a magnitude of up to 15 MHz and a period of about 300 s have been observed repeatedly for the WS6-600. The measurement is more often noisy at short exposure times of about 600 ms but above this limit, it is not susceptible to the exposure time (cf. color encoding in fig. A1) and also not to the laser's optical power, which was verified by another measurement at higher power (not shown here). We use this measurement as a reference, to deduce the accuracy of other wavemeters that we were not able to test against the iodine cell.

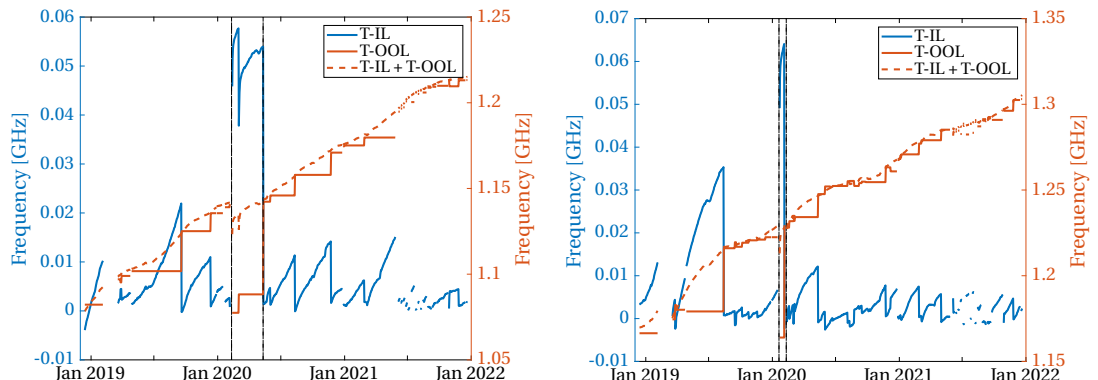
Appendix C. Calibration of OGSE laser and WS7-60

After calibrating the WS6-600 wavemeter, the laser of the OGSE was characterized w. r. t. its thermal coupling and drifts. The OGSE laser was used in single-spacecraft functional tests to simulate the received light for the LRI units, which the flight laser units will offset-lock their frequency to. At the integration facility, a second wavemeter, the WS7-60 with an absolute accuracy of 60 MHz, was available alongside the WS6-600. Hence, we will use this measurement to calibrate the WS7-60 against the WS6-600.

A comparison of the two wavemeters, shown in fig. A2, revealed that the WS6-600 measures frequencies which are lowered by approximately 40 to 80 MHz compared to the WS7-60. This is consistent to the calibration with iodine lines (see appendix B and fig. A1). It was found, that the OGSE laser needs at least 60 to 80 min to reach thermal equilibrium. The frequency drift after this warm-up phase is below 20 kHz/s. Since the two measurements agree well and the WS6-600 offset was observed before, it was concluded that the WS7-60 is accurate within the needs.

Appendix D. Thermal actuator signals of GF-1

Figure A3 illustrates the thermal actuator signals of the two LRI units. Highlighted between the black vertical lines are the regions, where the LRI locked before thermal equilibrium was reached, causing the in-loop signal to reach higher values than usual. At these instances, the telemetry-based laser frequency model shows nonphysical steps, which are then corrected by empirical parameters in eq. (44).



(a) GF-1 actuator signals. A step is visible at the first dashed vertical line, where the LRI locked before reaching thermal equilibrium. At the second vertical line, no frequency step is visible, but the actuator signals jumped back to the usual range.

(b) GF-2 actuator signals. Similar but smaller steps as in the left subplot are present between the two dashed vertical lines.

Figure A3. Control loop actuator signals multiplied with their calibrated coefficient (see table 1) for the thermal actuator of the Reference Laser Units (RLUs) from 2018-Dec until 2022-Jan. *Left axes:* In-loop (IL) signal (blue). *Right axes:* Out-of-loop (OOL) signal (orange) and sum of both (dashed orange). The black vertical lines indicate the times, where a step was applied in the empirical model.

Appendix E. LRI Time Frames

The LRI time frame is initialized at startup of the Laser Ranging Processor (LRP), however this initialization introduces an unknown offset of 1.5 s at maximum between the Onboard Computer (OBC) time and the LRI time. After initialization, the LRP clock is counting eight-

fold Ultra-Stable Oscillator (USO) ticks, which makes a clock rate of 38.656 000 MHz for GF-1 and 38.656 792 MHz for GF-2. This offset between the LRI time frame and the OBC time is determined regularly using so-called datation reports. The reported datation bias remains constant between reboots of either the LRP or the MWI Instrument Processing Unit (IPU). Furthermore, a filter is used inside the LRP to reduce the phase telemetry sampling rate to roughly 10 Hz. This filter introduces a delay of 28 802 038 clockticks (roughly 0.75 s, slightly different for the two spacecraft) that has to be accounted for [15,35]. In actual flight-data processing, correlating K-band Ranging (KBR) and LRI range data yields an estimated additional offset of approximately 75 μ s, whose origin is unknown and that is not measured with LRI datation reports.

References

1. Abich, K.; Abramovici, A.; Amparan, B.; Baatzsch, A.; Okihiro, B.B.; Barr, D.C.; Bize, M.P.; Bogan, C.; Braxmaier, C.; Burke, M.J.; et al. In-Orbit Performance of the GRACE Follow-on Laser Ranging Interferometer. *Physical Review Letters* **2019**, *123*. <https://doi.org/10.1103/physrevlett.123.031101>.
2. Landerer, F.W.; Flechtner, F.M.; Save, H.; Webb, F.H.; Bandikova, T.; Bertiger, W.I.; Bettadpur, S.V.; Byun, S.H.; Dahle, C.; Dobslaw, H.; et al. Extending the Global Mass Change Data Record: GRACE Follow-On Instrument and Science Data Performance. *Geophysical Research Letters*, *47*. <https://doi.org/10.1029/2020gl088306>.
3. Ghobadi-Far, K.; Han, S.C.; McCullough, C.M.; Wiese, D.N.; Yuan, D.N.; Landerer, F.W.; Sauber, J.; Watkins, M.M. GRACE Follow-On Laser Ranging Interferometer Measurements Uniquely Distinguish Short-Wavelength Gravitational Perturbations. *Geophysical Research Letters*, *47*. <https://doi.org/10.1029/2020gl089445>.
4. Conklin, J.; Yu, T.; Guzman, F.; Klipstein, B.; Lee, J.; Leitch, J.; Numata, K.; Petrov, S.; Spero, R.; Ware, B. LRI TechnologySummary and Roadmap for Mass Change Mission. Technical report, NASA Jet Propulsion Laboratory, 2020.
5. Massotti, L.; Siemes, C.; March, G.; Haagmans, R.; Silvestrin, P. Next Generation Gravity Mission Elements of the Mass Change and Geoscience International Constellation: From Orbit Selection to Instrument and Mission Design. *Remote Sensing* **2021**, *13*, 3935. <https://doi.org/10.3390/rs13193935>.
6. Nicklaus, K.; Cesare, S.; Massotti, L.; Bonino, L.; Mottini, S.; Pisani, M.; Silvestrin, P. Laser metrology concept consolidation for NGGM. In Proceedings of the International Conference on Space Optics — ICSO 2018; Karafolas, N.; Sodnik, Z.; Cugny, B., Eds. SPIE, 2019. <https://doi.org/10.1117/12.2536071>.
7. Amaro-Seoane, P.; Audley, H.; Babak, S.; Baker, J.; Barausse, E.; Bender, P.; Berti, E.; Binetruy, P.; Born, M.; Bortoluzzi, D.; et al. Laser Interferometer Space Antenna. <https://doi.org/10.48550/ARXIV.1702.00786>.
8. Sheard, B.S.; Heinzel, G.; Danzmann, K.; Shaddock, D.A.; Klipstein, W.M.; Folkner, W.M. Intersatellite laser ranging instrument for the GRACE follow-on mission. *Journal of Geodesy* **2012**, *86*, 1083–1095. <https://doi.org/10.1007/s00190-012-0566-3>.
9. Drever, R.W.P.; Hall, J.L.; Kowalski, F.V.; Hough, J.; Ford, G.M.; Munley, A.J.; Ward, H. Laser phase and frequency stabilization using an optical resonator. *Applied Physics B* **1983**, *31*, 97–105. <https://doi.org/10.1007/BF00702605>.
10. Thompson, R.; Folkner, W.M.; de Vine, G.; Klipstein, W.M.; McKenzie, K.; Spero, R.; Yu, N.; Stephens, M.; Leitch, J.; Pierce, R.; et al. A flight-like optical reference cavity for GRACE follow-on laser frequency stabilization. In Proceedings of the Joint Conference of the IEEE International Frequency Control and the European Frequency and Time Forum (FCS) Proceedings. IEEE, 2011. <https://doi.org/10.1109/fcs.2011.5977873>.
11. Spero, R. Point-mass sensitivity of gravimetric satellites. *Advances in Space Research*, *67*, 1656–1664. <https://doi.org/10.1016/j.asr.2020.12.019>.
12. Yan, Y.; Müller, V.; Heinzel, G.; Zhong, M. Revisiting the light time correction in gravimetric missions like GRACE and GRACE follow-on. *Journal of Geodesy*, *95*. <https://doi.org/10.1007/s00190-021-01498-5>.
13. Ashby, N.; Bertotti, B. Relativistic effects in local inertial frames. *Physical Review D* **1986**, *34*, 2246–2259. <https://doi.org/10.1103/physrevd.34.2246>.
14. Müller, V. Design Considerations for Future Geodesy Missions and for Space Laser Interferometry. PhD thesis, Leibniz Universität Hannover, 2017. <https://doi.org/10.15488/9029>.
15. Wen, H.Y.; Kruizinga, G.; Paik, M.; Landerer, F.; Bertiger, W.; Sakumura, C.; Bandikova, T.; McCullough, C. *GRACE-FO Level-1 Data Product User Handbook*. Jet Propulsion Laboratory, 2019. JPL D-56935, Version of September 11, 2019.
16. Misfeldt, M. Data Processing and Investigations for the GRACE Follow-On Laser Ranging Interferometer. Master's thesis, Leibniz Universität Hannover, 2019. <https://doi.org/10.15488/9639>.
17. Müller, V.; Hauk, M.; Misfeldt, M.; Müller, L.; Wegener, H.; Yan, Y.; Heinzel, G. Comparing GRACE-FO KBR and LRI ranging data with focus on carrier frequency variations. <https://doi.org/10.48550/ARXIV.2205.08862>.
18. Shiozawa, T. *Classical Relativistic Electrodynamics*; Springer Berlin Heidelberg, 2004. <https://doi.org/10.1007/978-3-662-06261-6>.

19. Wegener, H.; Müller, V.; Heinzel, G.; Misfeldt, M. Tilt-to-Length Coupling in the GRACE Follow-On Laser Ranging Interferometer. *Journal of Spacecraft and Rockets*, pp. 1–10. <https://doi.org/10.2514/1.a34790>.
20. Kornfeld, R.P.; Arnold, B.W.; Gross, M.A.; Dahya, N.T.; Klipstein, W.M.; Gath, P.F.; Bettadpur, S. GRACE-FO: The Gravity Recovery and Climate Experiment Follow-On Mission. *Journal of Spacecraft and Rockets* **2019**, *56*, 931–951. <https://doi.org/10.2514/1.A34326>.
21. Wen, H.Y. GRACE-FO L1 Release Notes.
22. Alnis, J.; Matveev, A.; Kolachevsky, N.; Udem, T.; Hänsch, T.W. Subhertz linewidth diode lasers by stabilization to vibrationally and thermally compensated ultralow-expansion glass Fabry-Pérot cavities. *Physical Review A*, **77**, 053809. <https://doi.org/10.1103/physreva.77.053809>.
23. Armano, M.; Audley, H.; Auger, G.; Baird, J.; Bassan, M.; Binetruy, P.; Born, M.; Bortoluzzi, D.; Brandt, N.; Caleno, M.; et al. LISA Pathfinder: First steps to observing gravitational waves from space. *Journal of Physics: Conference Series* **2017**, *840*, 012001. <https://doi.org/10.1088/1742-6596/840/1/012001>.
24. Pierce, R.; Stephens, M.; Kaptchen, P.; Leitch, J.; Bender, D.; Folkner, W.M.; Klipstein, W.M.; Shaddock, D.; Spero, R.; Thompson, R.; et al. Stabilized Lasers for Space Applications: A High TRL Optical Cavity Reference System. In Proceedings of the Conference on Lasers and Electro-Optics 2012. OSA, 2012.
25. Nicklaus, K.; Herding, M.; Baatzsch, A.; Dehne, M.; Diekmann, C.; Voss, K.; Gilles, F.; Guenther, B.; Zender, B.; Böhme, S.; et al. Optical bench of the laser ranging interferometer on grace follow-on. In Proceedings of the International Conference on Space Optics — ICSO 2014; Sodnik, Z.; Cugny, B.; Karafolas, N., Eds. International Society for Optics and Photonics, SPIE, 2017, Vol. 10563, pp. 738 – 746. <https://doi.org/10.1117/12.2304195>.
26. Müller, L. Generation of Level 1 Data Products and Validating the Correctness of Currently Available Release 04 Data for the GRACE Follow-On Laser Ranging Interferometer. Master's thesis, Leibniz Universität Hannover, 2021. <https://doi.org/10.15488/11818>.
27. Arie, A.; Schiller, S.; Gustafson, E.K.; Byer, R.L. Absolute frequency stabilization of diode-laser-pumped Nd:YAG lasers to hyperfine transitions in molecular iodine. *Opt. Lett.* **1992**, *17*, 1204–1206. <https://doi.org/10.1364/OL.17.001204>.
28. Döringshoff, K.; Schuldt, T.; Kovalchuk, E.V.; Stühler, J.; Braxmaier, C.; Peters, A. A flight-like absolute optical frequency reference based on iodine for laser systems at 1064 nm. *Applied Physics B*, **123**. <https://doi.org/10.1007/s00340-017-6756-1>.
29. Sanjuan, J.; Abich, K.; Blümel, L.; Gohlke, M.; Gualani, V.; Oswald, M.; Wegehaupt, T.; Schuldt, T.; Braxmaier, C. Simultaneous laser frequency stabilization to an optical cavity and an iodine frequency reference. *Optics Letters* **2021**, *46*, 360. <https://doi.org/10.1364/ol.413419>.
30. Rees, E.R.; Wade, A.R.; Sutton, A.J.; Spero, R.E.; Shaddock, D.A.; Mckenzie, K. Absolute frequency readout derived from ULE cavity for next generation geodesy missions. *Optics Express*, **29**, 26014. <https://doi.org/10.1364/oe.434483>.
31. Rees, E.R.; Wade, A.R.; Sutton, A.J.; Mckenzie, K. Absolute Frequency Readout of Cavity against Atomic Reference. *Remote Sensing*, **14**, 2689. <https://doi.org/10.3390/rs14112689>.
32. Schuldt, T. Frequenzstabilisierter Nd:YAG-Laser für Weltraumanwendungen. PhD thesis, Universität Hamburg, 2003.
33. Coherent, Inc.. Prometheus - Ultra-Narrow Linewidth CW DPSS Green Laser, 2022.
34. Riehle, F.; Gill, P.; Arias, F.; Robertsson, L. The CIPM list of recommended frequency standard values: guidelines and procedures. *Metrologia* **2018**, *55*, 188–200. <https://doi.org/10.1088/1681-7575/aaa302>.
35. Ware, B. LRI FM1 Datation Test Report. Technical report, Jet Propulsion Laboratory, California Institute of Technology, 2018.